PLANETARY SCIENCE

Fossil records of early solar irradiation and cosmolocation of the CAI factory: A reappraisal

David V. Bekaert[1,2]*, Maureen Auro[1], Quinn R. Shollenberger[3,4], Ming-Chang Liu[4], Horst Marschall[2,5,6], Kevin W. Burton[7], Benjamin Jacobsen[8], Gregory A. Brennecka[8], Glenn J. McPherson[9], Richard von Mutius[5], Adam Sarafian[1,2], Sune G. Nielsen[1,2]

Calcium-aluminum–rich inclusions (CAIs) in meteorites carry crucial information about the environmental conditions of the nascent Solar System prior to planet formation. Based on models of 50V–^{10}Be co-production by in-situ irradiation, CAIs are considered to have formed within ~0.1 AU from the proto-Sun. Here, we present vanadium (V) and strontium (Sr) isotopic co-variations in fine- and coarse-grained CAIs and demonstrate that kinetic isotope effects during partial condensation and evaporation best explain V isotope anomalies previously attributed to solar particle irradiation. We also report initial excesses of ^{10}Be and argue that CV CAIs possess essentially a homogeneous level of ^{10}Be, inherited during their formation. Based on numerical modeling of 50V–^{10}Be co-production by irradiation, we show that CAI formation during protoplanetary disk build-up likely occurred at greater heliocentric distances than previously considered, up to planet-forming regions (~1AU), where solar particle fluxes were sufficiently low to avoid substantial in-situ irradiation of CAIs.

INTRODUCTION

Astronomical observations of young stellar objects (YSOs) indicate that their surrounding accretionary disks are directly exposed to levels of x-ray and high-energy (≥10 MeV) particle emissions that are orders of magnitude higher than observed for most main-sequence stars (*1*, *2*). However, the duration and characteristics (gradual or impulsive flares) of these early stages of high stellar activity remain poorly understood. Anomalous abundances of short-lived radionuclides in Ca-Al–rich inclusions (CAIs) of carbonaceous chondrite meteorites have been suggested to be fossil records of dust irradiation by solar cosmic rays (SCRs) at the inner edge of the protoplanetary disk (PPD) (*3*). The most unambiguous evidence of CAI irradiation is the observation of ^{10}B excesses from the decay of ^{10}Be [$T_{1/2}$ = 1.386 ± 0.016 million years (Ma); (*4*)]—a short-lived radioactive isotope that exclusively requires a spallation origin—with initial ^{10}Be/^{9}Be ratios of (6 to 10) × 10^{-4} at the time of formation of CV3-chondrite CAIs (*5*–*10*). However, alternative models suggest that a fraction, if not all, of ^{10}Be in CAIs could have been inherited from a presolar stage, either via spallation reactions and trapping of galactic cosmic ray (GCR) ^{10}Be (*11*) or via irradiation of the presolar molecular cloud by background GCRs (*12*). Inheritance of ^{10}Be from early phases of nebular gas irradiation, before CAI formation, has also been proposed as a potential mechanism to account for most of ^{10}Be in CV CAIs (*13*). Reliable quantification of early solar irradiation processes from ^{10}Be records in meteorites is hampered by the lack of constraints regarding the nature of the target (nebular gas or proto-CAIs), as well as the duration and location of particle irradiation from the young Sun in the early Solar System.

Most CAIs originally formed as fine-grained condensates, with a subset experiencing episodes of remelting to form coarser igneous CAIs (*14*, *15*). That the mineralogical composition of fine-grained CAIs follows thermodynamic predictions of equilibrium condensation from a gas of approximately solar composition (*16*) supports the idea that CAIs condensed from the cooling gas phase of the PPD some 4567 Ma ago (*17*–*19*). The minerals they contain are rich in refractory elements (Ca, Al, Ti), indicating that they formed at temperatures over 1400 K, which would have mainly been reached near the proto-Sun. Physical models of ^{10}Be production in high-energy irradiation environments of the early Solar System have predicted that ^{50}V excesses of several per mil (‰) should be recorded in CAIs, whereby higher initial ^{10}Be/^{9}Be ratios would be associated with the largest V isotope anomalies (*3*, *20*). Recently, ^{50}V excesses up to 4.4‰ were reported in fine-grained CAIs and interpreted to covary with initial ^{10}Be abundances (*21*). Modeling of the coproduction of ^{50}V and ^{10}Be by in situ irradiation of proto-CAIs was taken to indicate that the dust was exposed to SCR associated with gradual flares at ~0.1 astronomical units (AU) from the proto-Sun for ≤300 years (*21*). Yet, CAIs are found to be most abundant (up to ~3 volume %) in meteorites that, based on their nucleosynthetic signatures (*22*, *23*), are considered to have accreted beyond the orbit of Jupiter. Unexpectedly, CAIs are extremely scarce (<0.2 volume %) in enstatite and ordinary chondrites, which most likely formed in the inner Solar System, closer to the surmised cosmolocation of the CAI factory (*24*). The anchoring of the CAI-forming region at the inner edge of the PPD therefore requires CAIs to have been efficiently transported to the outer regions of the Solar System, potentially above the disk midplane by stellar outflows (*3*, *25*) or at the disk midplane by a meridional flow (*24*, *26*). Precisely cosmolocating the CAI factory therefore has profound implications for our understanding of the structure and dynamical evolution of the PPD.

Although V has now emerged as a critical tool to constrain numerical models of dust irradiation by protosolar cosmic rays, it

[1]NIRVANA Laboratories, Woods Hole Oceanographic Institution, Woods Hole, MA 02543, USA. [2]Department of Geology and Geophysics, Woods Hole Oceanographic Institution, Woods Hole, MA 02543, USA. [3]Institut für Planetologie, University of Münster, Wilhelm-Klemm-Straße 10, Münster 48149, Germany. [4]Department of Earth, Planetary and Space Sciences, University of California, Los Angeles, CA 90095, USA. [5]Institut für Geowissenschaften, Goethe Universität, Altenhöferallee 1, 60438 Frankfurt am Main, Germany. [6]Frankfurt Isotope and Element Research Center, Goethe Universität, 60438 Frankfurt am Main, Germany. [7]Department of Earth Sciences, Durham University, Elvet Hill, Durham DH1 3LE, UK. [8]Nuclear and Chemical Sciences Division, Lawrence Livermore National Laboratory, Livermore, CA 94550, USA. [9]U.S. National Museum of Natural History, Smithsonian Institution, Washington, DC 20560, USA.
*Corresponding author. Email: dbekaert@whoi.edu

has only two stable isotopes (^{50}V and ^{51}V). Consequently, any unresolved contribution from nucleosynthetic and/or mass-dependent stable isotope fractionation effects could therefore potentially introduce a bias in our interpretations of V isotope variations in CAIs. Critically, multiple studies have demonstrated that CAIs contain substantial mass-dependent isotopic effects for the elements Ca, Si, Mg, Ti, Ni, Fe, Sr, and U due to processes such as evaporation, condensation, and gas-melt isotopic exchange during CAI formation [e.g., (*27*–*32*)]. Fortunately, the element Sr has a 50% condensation temperature [T_{50}(Sr) = 1464 K (*33*)] that is very close to that of V [T_{50}(V) = 1429 K (*33*)], and it has four stable isotopes—none of which is significantly produced by solar irradiation—hence greatly facilitating deconvolution of nucleosynthetic and kinetic fractionation effects (*31*). To investigate the potential for processes other than solar irradiation to induce V isotope variations in CAIs, here, we present the first coupled V and Sr isotope measurements in five coarse-grained and three fine-grained CAIs from the Allende CV3 meteorite (fig. S1 and table S1). In addition, for a subset of CAI samples, we present their ^{10}Be-^{10}B systematics and rare-earth element (REE) patterns. Our data reveal a clear V-Sr isotope correlation that follows predictions from kinetic isotope fractionation during partial condensation and evaporation and precludes a substantial influence of irradiation processes on the V isotope composition of CAIs. Using numerical modeling of ^{50}V and ^{10}Be coproduction by irradiation from the young Sun, we find that very little of the ^{10}Be in CV CAIs could have been produced via in situ irradiation in the vicinity of the proto-Sun. This result implies that most of ^{10}Be in CV CAIs was already present in the protosolar nebula when CAIs formed, and that the location of CAI formation need not have been as close to the proto-Sun as previously thought. Combining our findings with literature data, we re-evaluate the available records of early Solar System irradiation in meteorites and the associated constraints on the cosmolocation of the CAI factory in the nascent Solar System.

RESULTS

The V-Sr isotope correlation

Vanadium and strontium isotope compositions in CAIs are reported as parts per thousand (‰) deviations from the respective reference standards (Supplementary Materials), using the δ notation

$$\delta^{i}X = \left({}^{(i}X/{}^{j}X)_{\text{sample}} / {}^{(i}X/{}^{j}X)_{\text{reference}} - 1 \right) \times 1000 \quad (1)$$

where *i* and *j* denote isotopes of the element *X*. Consistent with previously reported V isotope data (*21*), we find δ^{51}V values that vary over >5‰ (Fig. 1). Fine-grained CAIs exhibit more negative δ^{51}V (ranging from −5 to −3‰) than coarse-grained CAIs (ranging from −2.5 to +0.5‰), which encompass the chondritic value [$\delta^{51}V_{\text{chondrite}}$ = −1.089 ± 0.031‰ (*34*)]. The heaviest V isotope composition measured here in CAI75 (δ^{51}V = +0.5‰) is the highest value ever reported in extraterrestrial matter. Furthermore, we find that δ^{88}Sr values also vary over a large range of ~5‰ (Fig. 1), which is similar to ranges previously reported for δ^{88}Sr variations in CAIs (*31*, *35*). When plotted in δ^{51}V versus δ^{88}Sr space (Fig. 1), six CAIs (five coarse-grained and one fine-grained) define a positive linear trend (R^2 = 0.995) that does not encompass the chondritic value.

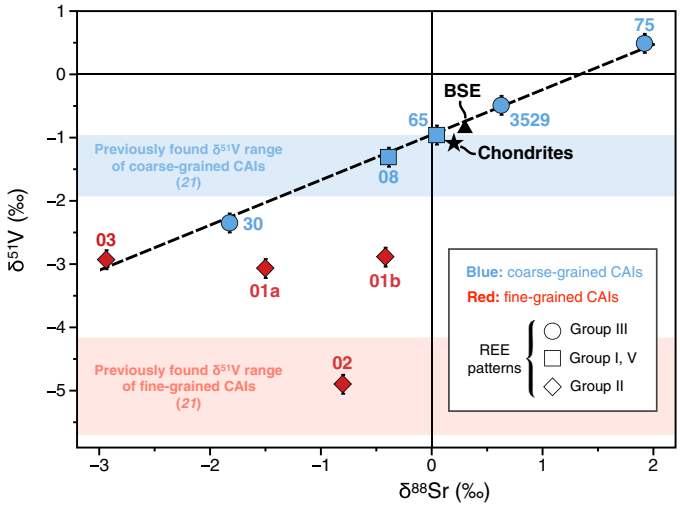

Fig. 1. δ^{51}V and δ^{88}Sr isotopic composition of fine- and coarse-grained CAIs (represented in red and blue, respectively). The dashed line represents the best fit of the linear regression through all coarse-grained CAIs and fine-grained CAI03 [$\delta^{51}V = (-0.956 \pm 0.092) + (0.715 \pm 0.056) \times \delta^{88}$Sr at 95% confidence interval (CI), $R^2 = 0.995$]. Ranges of δ^{51}V values previously measured by Sossi *et al.* (*21*) for fine- and coarse-grained CAIs are reported as red and blue areas, respectively. The bulk silicate earth (BSE) and chondritic compositions (*34*, *40*, *41*) are indicated by the black triangle and star, respectively. Numbers refer to individual sample labels (Supplementary Materials). Data points represented with circle, square, and diamond symbols refer to group III, group I, V, and group II RRE patterns, respectively (Supplementary Materials). Two fragments (labeled a and b) were analyzed for CAI01. Errors are given as 2σ.

The latter plots below the observed δ^{51}V-δ^{88}Sr correlation line, corresponding to a ~0.3‰ shift toward low δ^{51}V values (or ~0.4‰ shift toward high δ^{88}Sr values). In addition to the fine-grained CAI that plots on this correlation line, two analyzed fine-grained inclusions (CAI01 and CAI02) plot significantly below the δ^{51}V-δ^{88}Sr trend (Fig. 1). The two fragments we analyzed for CAI01 (labeled a and b in Fig. 1) have distinct δ^{88}Sr but indistinguishable δ^{51}V, suggesting perturbation of their δ^{88}Sr.

REE patterns

The different groups of CAI REE patterns observed here are summarized in the Supplementary Materials (fig. S2) and interpreted following Ireland and Fegley (*36*). Coarse-grained CAI08 and CAI65 have flat chondrite-normalized REE patterns (group I, V). Three coarse-grained CAIs (CAI3529, CAI75, and CAI30) have group III REE patterns characterized by depletions in the two most volatile REEs, europium (Eu) and ytterbium (Yb). The three fine-grained CAIs (CAI01, CAI02, and CAI03) show fractionated group II REE patterns thought to represent the "primitive" signature of nebular gas condensation (*37*).

Be-B measurements

Four coarse-grained CAIs were analyzed for Be-B isotopes by secondary ion mass spectrometry. During these measurements, extra care was taken to eliminate sample contamination by terrestrial boron in the analyzed CAIs (figs. S5 to S9). All four CAIs show evidence for the presence of short-lived ^{10}Be at the time of their

formation (Fig. 2). Sample CAI75 presents high $^{9}Be/^{11}B$ (up to ~600), as well as extremely low boron concentrations (<1 ng/g). The three other samples show higher boron concentrations in the range of 50 to 120 ng/g (Supplementary Materials). Initial $^{10}Be/^{9}Be$ (noted $^{10}Be/^{9}Be_0$) and $^{10}B/^{11}B$ (noted $^{10}B/^{11}B_0$) derived for the four isochrons presented here are within the range of previously published data for CAIs in CV chondrites [e.g., (*5*–*8*, *21*)]. $^{10}Be/^{9}Be_0$ for CAI75 and CAI08 (~7×10^{-4}), which both exhibit $^{9}Be/^{11}B > 100$, are close to typical values obtained for CV CAIs [~8×10^{-4} (*8*)]. ^{10}Be-^{10}B isochrons for CAI65 and CAI3529 are defined over more restricted ranges of $^{9}Be/^{11}B$ values (≤9.11 and ≤0.23, respectively). The $^{10}Be/^{9}Be_0$ derived for CAI3529 (~9×10^{-3}) is similar to the value of 7×10^{-3} reported by Sossi *et al.* (*21*), with both isochrons being defined over small $^{9}Be/^{11}B$ ranges [≤1.5 for Sossi *et al.* (*21*)] and being associated with high mean square weighted deviation (MSWD) values, therefore pointing toward an overdispersion of the data (*38*). Different fragments of CAI3529 have been previously analyzed for Be-B, yielding maximum $^{9}Be/^{11}B$ values ranging from ≤5 (CAI3529–30) up to 200 (CAI3529–41) (*5*, *8*). The analysis of the latter fragment provided one of the best-defined $^{10}Be/^{9}Be_0$ ever determined in CAIs, at $(8.6 \pm 0.6) \times 10^{-4}$ (*5*, *8*).

Rb-Sr systematics

Rb/Sr ratios in CAIs are generally highly variable, with fine-grained CAIs typically displaying elevated values consistent with the introduction of chondritic Rb (and so most likely chondritic Sr, albeit to a lesser degree) into the CAIs by alkali-rich secondary alteration fluids (*31*). ^{87}Sr variations in CAIs are primarily controlled by the radiogenic decay of long-lived ^{87}Rb [$T_{1/2}$ ~ 50×10^{9} years (*39*)]. The low $^{87}Rb/^{86}Sr$ ratios and primitive $^{87}Sr/^{86}Sr$ (<0.702) observed for all coarse-grained CAIs investigated here indicate that the influence of aqueous alteration on their Sr isotope compositions has remained limited. Conversely, $^{87}Sr/^{86}Sr$ up to ~0.744 in fine-grained CAIs points to substantial secondary addition of Rb. For example, CAIs 01 (a and b) and 02, which do not plot on the $\delta^{51}V$-$\delta^{88}Sr$ correlation (Fig. 1), have $^{87}Sr/^{86}Sr \geq 0.73$ (Supplementary Materials). Qualitatively, our data indicate a first-order distinction between (i) CAIs exhibiting primitive $^{87}Sr/^{86}Sr$ and plotting on the $\delta^{51}V$-$\delta^{88}Sr$ correlation line and (ii) those that show evidence for radiogenic ingrowth of ^{87}Sr from ^{87}Rb of secondary origin and do not plot on the $\delta^{51}V$-$\delta^{88}Sr$ correlation line. One exception to this is the fine-grained CAI03, which is on the $\delta^{51}V$-$\delta^{88}Sr$ correlation and displays an elevated $^{87}Sr/^{86}Sr$ (~0.729; Supplementary Materials). CAI02, which exhibits the highest $^{87}Sr/^{86}Sr$ (~0.744; Supplementary Materials), shows most deviation from the $\delta^{51}V$-$\delta^{88}Sr$ correlation line (Fig. 1). The two fragments we analyzed for CAI01 (labeled a and b in Fig. 1) have distinct $\delta^{88}Sr$ (but similar $\delta^{51}V$), pointing to a heterogeneous $\delta^{88}Sr$. All CAIs analyzed in this study roughly plot within the errorchron 2σ-envelope defined by coarse-grained CAIs (fig. S3). However, because of the large dispersion of the data, this errorchron has limited geochronological meaning. Its slope provides a poorly defined age of 4.1 ± 0.7 Ga, with an initial $^{87}Sr/^{86}Sr = 0.69904 \pm 0.00062$ (2σ; fig. S3), which is indistinguishable from the canonical $^{87}Sr/^{86}Sr$ of CAIs [0.69886 ± 0.00020 (*31*)].

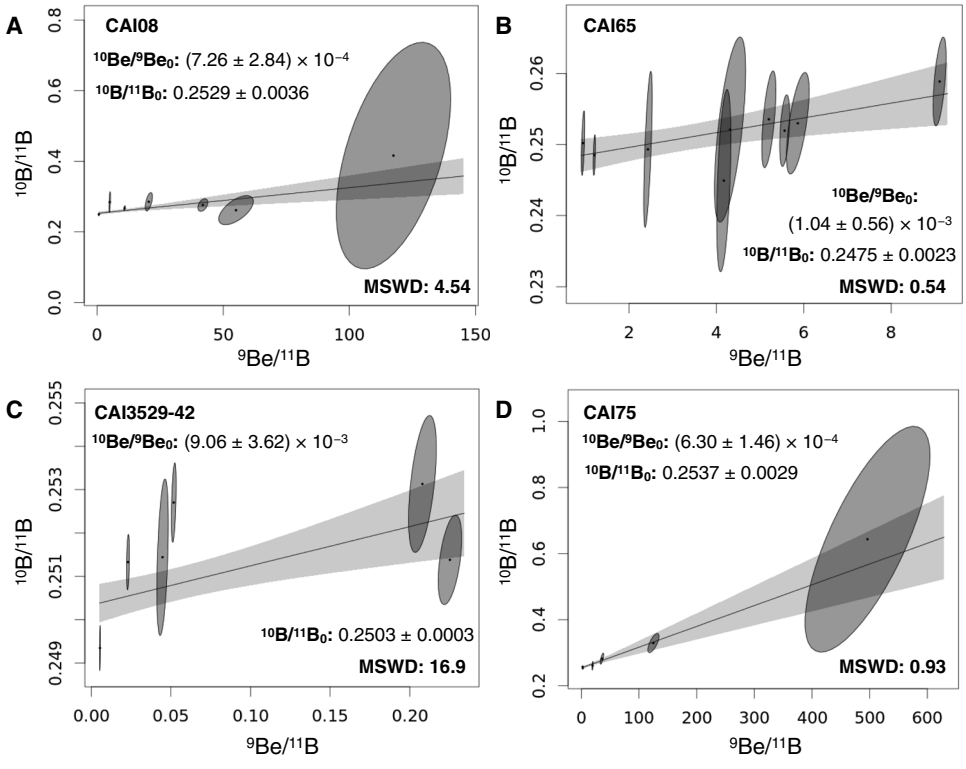

Fig. 2. ^{10}Be-^{10}B isochrons of coarse-grained CAIs analyzed in this study. Samples CAI08, CAI65, CAI3529–42, and CAI75 are shown in panels (**A**), (**B**), (**C**), and (**D**), respectively. In each panel, the solid line and associated 2σ envelope represent the error-weighted least square fit through the data (*90*). Corresponding slopes and *y* intercepts are reported together with MSWD values. Chondritic $^{10}B/^{11}B$: 0.2481 (*91*). All uncertainties are given as 2σ.

DISCUSSION

V-Sr isotope systematics in CAIs

The strong correlation between $\delta^{51}V$ and $\delta^{88}Sr$ for five coarse-grained and one fine-grained CAIs (Fig. 1) suggests that V and Sr isotopic variations in CAIs are primarily controlled by a common process. Given that V and Sr behave differently geochemically (due to large differences in ionic charge and radius), but have comparable 50% condensation temperatures (*33*), this $\delta^{51}V$-$\delta^{88}Sr$ correlation could have a volatility-controlled origin. In agreement with Mg, Ca, and Fe systematics in CAIs [e.g., (*32*)], V and Sr indicate that fine-grained CAIs are generally isotopically lighter than igneous CAIs, which most likely reflects the fact that igneous CAIs experienced more substantial evaporation, as these CAIs were once molten, driving their isotopic compositions toward heavier values. A $\delta^{51}V$-$\delta^{88}Sr$ relationship could, in principle, be controlled by a number of processes, such as (i) secondary alteration of fine-grained CAIs, (ii) irradiation processes, (iii) equilibrium isotope fractionation, and/or (iv) nucleosynthetic anomalies. Below, we show that (v) kinetic fractionation during evaporation/condensation is the main process controlling $\delta^{51}V$-$\delta^{88}Sr$ variations in CAIs.

(i) Secondary alteration of fine-grained CAIs

Contrary to V, nucleosynthetic, radiogenic, and stable Sr isotopic variations in fine- and coarse-grained CAIs have been extensively investigated. Refractory inclusions recently analyzed by Charlier *et al.* (*31*) exhibit a range of $\delta^{88}Sr$ values of ~5.3‰ (−3.67 to +1.67‰) that reflect kinetic isotope effects during partial condensation/evaporation and/or low-temperature alteration processes. Here, we find that the CAIs showing least evidence for pervasive addition of Rb during secondary alteration (i.e., coarse-grained CAIs; Supplementary Materials) plot on the $\delta^{51}V$-$\delta^{88}Sr$ correlation. Conversely, fine-grained CAIs 01 and 02, which depart from the $\delta^{51}V$-$\delta^{88}Sr$ correlation line, exhibit high $^{87}Sr/^{86}Sr$ and $^{87}Rb/^{86}Sr$, reflecting secondary addition of Rb and partial equilibration of the $\delta^{88}Sr$ with aqueous fluids of chondritic composition [i.e., $\delta^{88}Sr$ = 0.2‰ (*40*, *41*)]. The fact that the two fragments analyzed for CAI01 (labeled a and b in Fig. 1) have distinct $\delta^{88}Sr$ but similar $\delta^{51}V$ reinforces our interpretation that the deviation of CAI01 (and likely CAI02) from the $\delta^{51}V$-$\delta^{88}Sr$ correlation line arises from internal heterogeneities in $\delta^{88}Sr$ and not $\delta^{51}V$. In this framework, the $\delta^{88}Sr$ of CAIs 01 and 02 would not reflect their primordial compositions. As observed in terrestrial contexts [e.g., (*42*)], Rb and Sr may be decoupled during alteration [e.g., (*31*)] such that the occurrence of high $^{87}Sr/^{86}Sr$ (reflecting secondary addition of Rb) may not necessarily imply that the $\delta^{88}Sr$ of the corresponding CAI was perturbed during aqueous fluid circulation. Hence, $^{87}Sr/^{86}Sr$ variations may only provide a first-order, qualitative indication regarding whether or not aqueous alteration affected the corresponding CAIs. Hydrothermal fluids do not mobilize V, and so, its isotopic composition is not modified beyond analytical uncertainty by pervasive hydrothermal alteration processes (*43*). Although some of the CAIs plotting on the $\delta^{51}V$-$\delta^{88}Sr$ correlation likely experienced some degree of secondary alteration (e.g., CAI03; fig. S3), their occurrence on the $\delta^{51}V$-$\delta^{88}Sr$ correlation (Fig. 1) suggests that potential aqueous processes had a negligible effect on their stable Sr isotope compositions. Notably, we cannot exclude the possibility that the primordial $\delta^{88}Sr$ of CAI03 was more negative than observed today by up to several per mil, as suggested by the large deviations of CAIs 01 and 02 from the correlation line (Fig. 1). However, such a scenario would imply that subsequent disruption of the $\delta^{88}Sr$ by equilibration with the aqueous fluid and potential production of ^{50}V by irradiation processes fortuitously drove the $\delta^{51}V$-$\delta^{88}Sr$ composition of CAI03 on the correlation line defined by other CAIs. In this case, the fact that CAI03 plots on the $\delta^{51}V$-$\delta^{88}Sr$ correlation line would be circumstantial. Although we cannot rule out this possibility, we consider that the available dataset is not sufficient to justify excluding CAI03 from the correlation line. Charlier *et al.* (*31*) demonstrated that the distributions of Rb and Sr between fine- and coarse-grained CAIs are largely decoupled. Contrary to theoretical expectations, these authors showed that Sr and Eu abundances in fine-grained CAIs are strongly coupled, which suggests that the distribution of Sr in fine-grained CAIs reflects not only introduction of Sr by aqueous alteration but also variable extents of incomplete condensation from nebular gas. Future investigations of coupled $\delta^{51}V$-$\delta^{88}Sr$ and $^{87}Rb/^{86}Sr$-$^{87}Sr/^{86}Sr$ systematics have the potential to shed further light on the mechanisms controlling $\delta^{88}Sr$ variability in fine-grained CAIs. Here, we consider that the CAIs plotting on the $\delta^{51}V$-$\delta^{88}Sr$ correlation (Fig. 1) most likely preserved the primordial stable Sr isotope composition produced by condensation and evaporation processes in the PPD.

(ii) Irradiation processes

Given that stable Sr isotope compositions are unaffected by irradiation (*31*), and the fact that production of ^{50}V by irradiation would only lower the $\delta^{51}V$ values in CAIs, irradiation alone cannot account for the observed $\delta^{51}V$-$\delta^{88}Sr$ correlation (Figs. 1 and 3). Therefore, the strong $\delta^{51}V$-$\delta^{88}Sr$ correlation dictates that little (<0.2‰), if any, V isotope variation arises from irradiation processes. Although additional data would be required to test this interpretation, the fact that the chondritic value in V-Sr isotope space plots ~0.3‰ below the CAI correlation line (Fig. 1) could suggest that the gas reservoir from which chondrites formed was enriched in ^{50}V by ~0.3‰ with respect to the gas reservoir from which CAIs condensed. The exact timing of CAI formation relative to other chondritic components is unclear: Whereas ^{26}Al-^{26}Mg systematics suggest a gap of 2 to 3 Ma (and up to 3 to 4 Ma for CR meteorites) between the formation of CAIs and that of chondrules (*44*), ^{207}Pb-^{206}Pb data for chondrules indicate a range of ages with essentially no temporal gap (*45*). In any case, at a given time of the PPD evolution, ^{50}V production by irradiation would have decreased with heliocentric distance [e.g., (*21*)], which is the opposite of what would be required to produce ^{50}V enrichments in chondrules and other chondrite matrix material relative to CAIs. Enstatite, ordinary, Rumuruti, and carbonaceous chondrites, thought to have accreted within a relatively short time span and at highly variable heliocentric distances (*24*), all have indistinguishable V isotope compositions (*34*). If dust exposure to solar irradiation was the main process with substantial effect on the V isotope composition of Solar System materials, then distinct chondritic groups could have received variable amounts of solar irradiation and therefore ended up with different bulk V isotope compositions, which is not observed (*34*). Furthermore, the bulk abundance of CAIs, which are the most likely carriers of irradiation-induced V isotope anomalies (*21*), greatly varies across different chondritic groups (*24*). Yet, all the chondrites analyzed so far display uniform bulk V isotope compositions (*34*), indicating that the V isotopic heterogeneity that exists among CAIs does not influence the isotopic composition of bulk chondrites.

(iii) Nucleosynthetic anomalies

Nucleosynthetic isotope anomalies in bulk meteorites have been observed for a large number of elements [e.g., Ti, Sr, Ca, Cr, Ni, Mo,

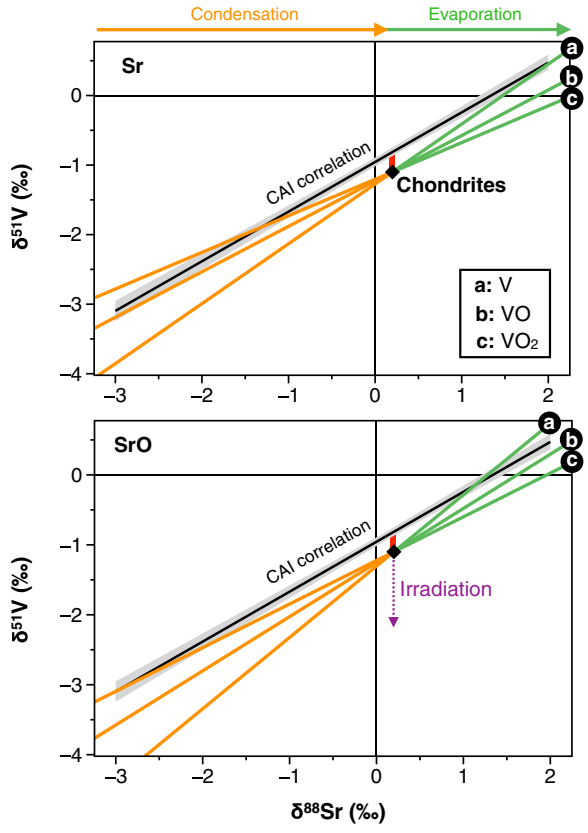

Fig. 3. Condensation (orange) and evaporation (green) isotopic trends expected in δ^{51}V-δ^{88}Sr space, starting from a nebular gas of chondritic composition and assuming that V and Sr species have identical sticking coefficients (γ_i) and 50% condensation temperatures (T_{50}). The different trends represent the various potential combinations of V and Sr atomic and molecular species (i.e., V, VO, VO_2 and Sr, SrO, respectively) that may be expected in the PPD (*53*). The solid black line and its gray envelope represent the CAI correlation line presented in Fig. 1. It is noteworthy that the slope of the δ^{51}V-δ^{88}Sr correlation line may be readily reproduced by considering Sr in atomic form and V as 64% VO and 36% V. The vertical red line emphasizes a shift of ~0.3‰ between the chondritic composition and the CAI correlation line. The purple arrow shows the effect of irradiation processes, which would only tend to lower δ^{51}V values due to cosmogenic ^{50}V production.

and Ru (*46*)]. Together, these indicate that the bulk isotope composition of carbonaceous chondrites is generally offset from that of noncarbonaceous chondrites toward the composition of CAIs (*46*, *47*). Although V isotope compositions of bulk carbonaceous chondrites have been proposed to broadly correlate with nucleosynthetic anomalies of ^{54}Cr (*48*), subsequent studies have found that V isotope variations in bulk chondrites can be ascribed to recent production of ^{50}V from GCR spallation processes (*49*). Once corrected for this effect, V isotope data for all types of chondrites investigated to date display a uniform composition (*34*). The lack of V isotope variation in chondritic bodies that accreted over a large range of heliocentric distances implies that nucleosynthetic V isotope anomalies, if they exist, are negligible. The absence of V nucleosynthetic anomalies in meteorites appears in line with the fact that the two isotopes of V are synthesized by a common process [explosive oxygen burning (*50*)]. This concept is greatly bolstered by a lack of V isotopic variation in sequential acid leaching experiments we have here carried out on the Murchison CM2 chondrite (Supplementary Materials). These leaching experiments classically provide large isotopic variation by chemically isolating heterogeneously distributed presolar components present in primitive chondrites [e.g., (*46*)]. The lack of V isotope variation during the progressive dissolution of the Murchison carbonaceous chondrite (Supplementary Materials) provides further evidence for the absence of significant V nucleosynthetic anomalies across the Solar System.

(iv) Equilibrium isotope fractionation

Theoretically, the equilibrium isotopic fractionation (also called reduced partition function ratio) between two compounds can be calculated from the vibrational energies of the bonds in each isotopic species [e.g., (*51*)]. However, these data are, to our knowledge, not available for the likely species involved in condensing or evaporating the two elements (V and Sr) considered in this study. The extent of equilibrium isotopic fractionation of V and Sr during condensation or evaporation of CAIs, where the magnitude of fractionation is primarily controlled by the transformation reaction from vapor to solid phase(s), is therefore unknown. Given the elevated temperature involved in CAI formation, the common assumption is that equilibrium isotopic fractionation should, however, be small (*15*). In the case of Ca, for example, small positive mass-dependent isotope effects of up to <0.5‰ can be produced by equilibrium fractionation (*52*). This is because, under nebular conditions, Ca is present in its atomic form in the gas phase, and Ca bonded to other atoms in the condensate favors the heavy isotopes. On the other hand, elements such as Ti, which are bonded to oxygen (as TiO and/or TiO_2), have much more similar bond strengths between the gas and solid phases even when Ti occurs in different oxidation states, therefore resulting in smaller equilibrium isotopic fractionation effects (*52*). Under nebular conditions, dominant V-bearing gas species are, like for Ti, associated with at least one atom of oxygen [VO, VO_2, and V_4O_{10} (*53*)], which therefore limits the potential for substantial equilibrium fractionation of V isotopes. As for Sr, it could have been equally present as Sr and SrO in the gas phase of the PPD (*53*), which could theoretically produce small (likely <0.5‰) equilibrium fractionation effects. However, such a process would not be able to explain the Sr-V isotope correlation (Fig. 1) and the magnitudes of potential equilibrium isotope fractionation effects for both elements are at least an order of magnitude smaller than the overall V-Sr isotopic variations observed here.

(v) Kinetic fractionation during evaporation/condensation

In the following, we show that the observed covariation of V and Sr isotopes in CAIs, as well as their offset from the chondritic values (Fig. 1), can be readily explained by kinetic isotopic fractionation during evaporation and condensation, as mathematically formulated by Richter (*54*) (Supplementary Materials). In this framework, it is assumed that the gas phase starts with a chondritic isotope composition and is dominated by a single species containing the element of interest. We note that the atomic form of V is considered here in the modeling for the purpose of comparison, but it is not expected to be a dominant V-bearing species within the gas phase of the protosolar nebula (*53*). Conversely, we do not consider gaseous V_4O_{10}, as the widespread occurrence of this species would require conditions that are far more oxidizing than the canonical protosolar nebula. The equations we use follow the usual formulation of the Rayleigh fractionation, whereby f is the fractional amount of a given isotope remaining in the source (gas phase for condensation and solid phase for evaporation), α is the kinetic isotope fractionation factor,

and γ_i is the "sticking" (or "evaporation") coefficient (Supplementary Materials). The formalism of this approach relies on the fact that condensation/evaporation kinetics are governed by thermodynamics and equilibrium vapor pressures through the Hertz-Knudsen equation (*55*)

$$J_i = \frac{n\,\gamma_i\,(P_{i,\mathrm{sat}} - P_i)}{\sqrt{2\pi\, m_i RT}} \quad (1)$$

where J_i is the flux of i in moles per unit area per unit time (i.e., net evaporation regime if $J_i > 0$), n is the number of atoms of i in the dominant gas species molecule containing i, γ_i is the dimensionless sticking coefficient for i, $P_{i,\mathrm{sat}}$ and P_i are the saturation vapor pressure and partial pressure of the gas molecule containing i at the surface of the condensed phase, m_i is the molecular mass of species i, R is the ideal gas constant, and T is the absolute temperature (*54*). This approach therefore makes the simplifying assumption that the gas phase is dominated by a single species containing one atom of the element of interest. Close to equilibrium conditions (i.e., when P_i approaches $P_{i,\mathrm{sat}}$), the net flux tends toward zero. As considered here below, the net flux becomes maximal close to free evaporation conditions, also referred to as the "vacuum limit" (i.e., when $P_i << P_{i,\mathrm{sat}}$).

First, we assume that V and Sr species have identical γ_i and T_{50} and so identical f during condensation and evaporation. Theoretical traces of the V and Sr isotopic evolution of the CAIs during partial condensation and evaporation are represented in Fig. 3 for the different atomic or molecular species considered here for V and Sr. We observe that the slopes of these condensation and evaporation lines (i) vary depending on the Sr/SrO and V/VO/VO_2 of the gas and (ii) are all relatively close to the actual δ^{51}V-δ^{88}Sr correlation line of CAIs (Fig. 3). In theory, it is possible to adopt distinct sticking coefficient ratios for the isotopes of Sr and V (e.g., $\gamma^{50}V = \gamma^{51}V$ and $\gamma^{86}Sr = 0.9976 \times \gamma^{88}Sr$) to force each one of these isotopic traces to reproduce the slope of the CAI correlation line (Supplementary Materials). However, any scenario considering identical f for the V and Sr species will produce condensation/evaporation lines that unavoidably pass through the chondritic value (Fig. 3), as opposed to the actual δ^{51}V-δ^{88}Sr correlation line of CAIs, which is offset from chondrites by ~0.3‰ toward high δ^{51}V values. Likewise, different combinations of these atomic or molecular species would allow reproducing the slope of the CAI δ^{51}V-δ^{88}Sr correlation line (e.g., considering Sr in atomic form and V as 64% VO and 36% V) but not its offset from chondrites. Below, we show that considering identical sticking/evaporation coefficient ratios for the isotopes of V and Sr (i.e., $\frac{\gamma^{50}V}{\gamma^{51}V} = \frac{\gamma^{86}Sr}{\gamma^{88}Sr} = 1$), but slightly different volatilities for V and Sr (hereafter interpreted in terms of differences in their T_{50} as we make the simplifying assumption that $\gamma_V = \gamma_{Sr}$), naturally produces the observed offset between chondrites and the CAI correlation line as long as <100% of the nebular gaseous V and Sr of chondritic composition is initially condensed.

For each combination of V and Sr species considered here (Fig. 3), we compute the linear functions that relate f(V) and f(Sr), during either condensation or evaporation, and enable exactly reproducing the δ^{51}V-δ^{88}Sr correlation line of CAIs (Table 1 and Supplementary Materials). These linear functions [written in the form $f(V) = a \times f(Sr) + b$, where a and b are two constants] can be used to explain the V and Sr isotope composition of all CAIs belonging to the correlation line observed in Fig. 1, starting from nebular gas of chondritic composition. These equations demonstrate that kinetic fractionation during evaporation/condensation is able to readily explain the full range of primordial V and Sr isotope compositions in coarse-grained CAIs, with no requirement for irradiation, nucleosynthetic, or equilibrium fractionation contributions. Further interpreting these linear functions in terms of condensation/evaporation thermodynamics is, however, hampered by the lack of constraints regarding the condensation profiles of V and Sr. Thermodynamic condensation model curves have been established in the literature for major elements such as Si, Mg, Ca, Ti, and Al (Fig. 4) (*52*, *56*). These curves present distinct slopes (with the steepness of Si < Al < Ti) and, eventually, some kinks (e.g., for Si and Ca) corresponding to the condensation of mineral phases into which the considered element strongly partitions. Given the exceptionally strong correlation between δ^{88}Sr and δ^{51}V in CAIs, it appears reasonable to assume that V and Sr would have roughly

Table 1. Summary table of the *f* (V) – *f* (Sr) linear functions required to reproduce the CAI correlation line in δ^{51}V-δ^{88}Sr space, starting from a nebular gas of chondritic composition. Given that the fractionation factor between two isotopes/isotopologs depends on the inverse square root of their respective masses (Supplementary Materials), considering different V- and Sr-bearing species produces condensation/evaporation lines with variable slopes in δ^{51}V-δ^{88}Sr space. To reproduce the δ^{51}V-δ^{88}Sr correlation line observed in CAIs from the variable slopes presented in Fig. 3 therefore requires the difference in volatility between the two considered elements to be adjusted. For each combination of V- and Sr-bearing species (*53*), we numerically search for the f (V) – f (Sr) linear relationship that enables reproducing the δ^{51}V-δ^{88}Sr correlation line observed in CAIs. Assuming that $\gamma_V = \gamma_{Sr}$, we compute the modeled range of ΔT_{50}(V-Sr) values during condensation, here reported in italic (see Fig. 4).

		V	VO	VO_2
Condensation	Sr	$f(V) = 0.6781 \times f(Sr) + 0.3274$	$f(V) = 1.0513 \times f(Sr) - 0.0406$	$f(V) = 1.5051 \times f(Sr) - 0.4871$
	ΔT_{50} (V-Sr)	*+6 to +25 (K)*	*−1 to 0 (K)*	*−16 to −4 (K)*
	SrO	$f(V) = 0.5112 \times f(Sr) + 0.4932$	$f(V) = 0.7927 \times f(Sr) + 0.2162$	$f(V) = 1.1350 \times f(Sr) - 0.1196$
	ΔT_{50} (V-Sr)	*+13 to +49 (K)*	*+4 to +14 (K)*	*−5 to −1 (K)*
Evaporation	Sr	$f(V) = 0.8130 \times f(Sr) + 0.1597$	$f(V) = 1.0437 \times f(Sr) - 0.0796$	$f(V) = 1.2630 \times f(Sr) - 0.3076$
	SrO	$f(V) = 06947 \times f(Sr) + 0.2780$	$f(V) = 0.8919 \times f(Sr) + 0.0722$	$f(V) = 1.0794 \times f(Sr) - 0.1238$

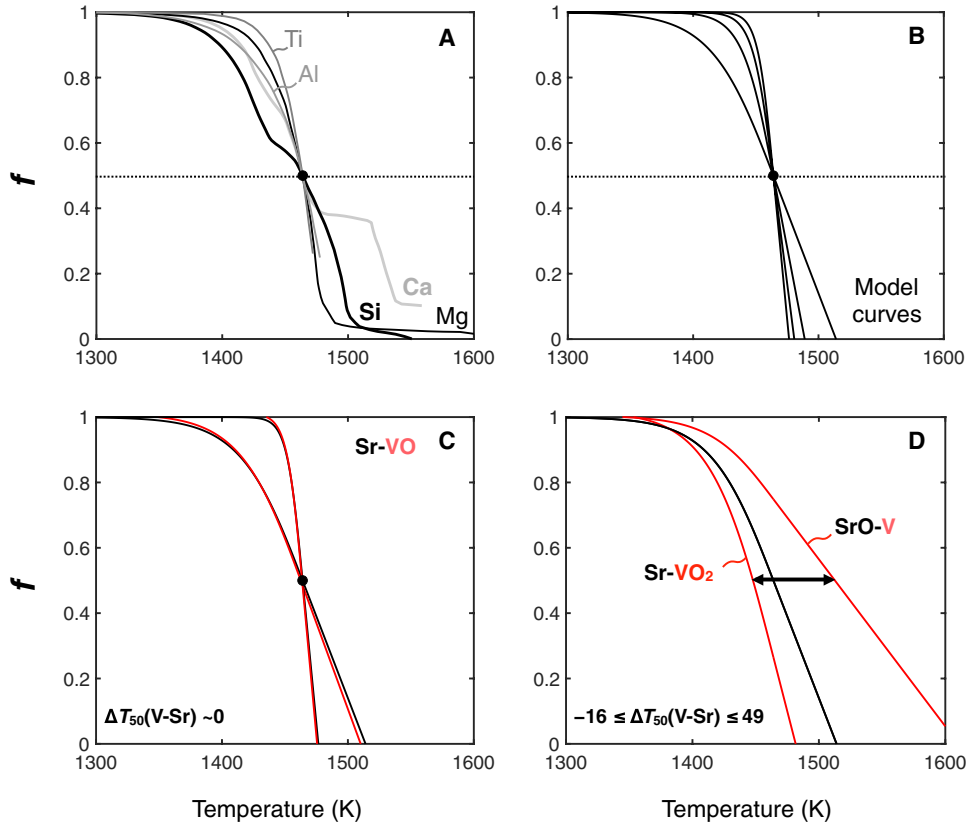

Fig. 4. A priori approach aimed at constraining the potential difference between the T_{50} of V and Sr using the (V) – (Sr) linear functions required to reproduce the δ^{51}V-δ^{88}Sr CAI correlation line. (**A**) Expected condensation curves of major elements [Ca, Si, Mg, Ti, and Al; (*52*)] normalized to a T_{50} of 1464 K. (**B**) Condensation curve profiles used in the present study to investigate potential differences between the T_{50} of V and Sr (see main text). These different profiles allow investigating condensation curves spanning the entire range of slopes observed for major elements. (**C**) The two black curves represent the two most extreme scenarios for the potential slope of the Sr condensation curve. Expected VO condensation curves are then built based on Table 1 [f(V) = 1.0513 × f(Sr) – 0.0406]. In this case, similar condensation curves for Sr and VO would be required to explain the δ^{51}V-δ^{88}Sr correlation line observed in CAIs [ΔT_{50}(V-Sr) ~ 0; Table 1]. (**D**) The two red curves represent the expected condensation curves of VO_2 and V in the case of Sr-VO_2 and SrO-V binary systems, respectively (Table 1). The black line corresponds to the condensation line of the Sr-bearing species. In this case (most gentle slope), ΔT_{50}(V-Sr) range from −16 K to +49 K.

similar condensation profiles but potentially different T_{50}. In addition, it is noteworthy that V and Sr are presumed to both condense as titanates/perovskite from nebular gas [e.g., $SrTiO_3$ (*33*, *57*)], suggesting that they behave concordantly during condensation in the protosolar nebula.

Here, we adopt an a priori approach to investigate the potential difference between the T_{50} of V and Sr using the linear functions presented in Table 1. In the interest of simplification, we built a numerical model generating smoothed condensation profiles that mimic the thermodynamic condensation model curves of major elements (Fig. 4) (*52*). First, we generate a series of smoothed Sr condensation profiles [f(Sr) as a function of temperature] that span the range of slopes observed for major elements. All curves for Sr are anchored to a T_{50} of 1464 K (*33*). Note that T_{50} values are specific to the precise thermodynamic conditions of the protosolar nebula, and so, they are not necessarily applicable to inferred conditions for CAI condensation/evaporation (*58*). Hence, we stress that the absolute T_{50} values are of little relevance here, as we are not building a thermodynamic model but rather investigating the relative difference between the T_{50} of V and Sr. Then, we generate, for each one of these Sr condensation curves, the six possible V condensation curves defined by the linear functions relating f (V) and f (Sr) (Table 1). The T_{50} of the so-produced V condensation curves are finally compared with the T_{50} of Sr to compute ΔT_{50}(V-Sr) values, corresponding to the differences between the modeled T_{50} of V and Sr [ΔT_{50}(V-Sr) = T_{50}(V) − T_{50}(Sr); Supplementary Materials]. Using this approach, we obtain ΔT_{50}(V-Sr) in the range −16 K to +49 K, which is in agreement with the T_{50} of V and Sr being very similar to one another (*33*). This finding is, however, different from thermodynamical considerations of VO, V_2O_3, and SrO condensation temperatures for ideal solid solution in perovskite (*59*), which suggested ΔT_{50}(V-Sr) in the range +130 to +267 K. Likewise, more recent calculations by Wood *et al.* (*57*) have proposed T_{50}(V) = 1370 K and T_{50}(Sr) = 1548 K, corresponding to a ΔT_{50}(V-Sr) of −178 K. Although it is likely that our simple approach does not capture the diversity of thermodynamical and physicochemical conditions associated with kinetic processes during CAI condensation and evaporation, our results are, at first approximation, most compatible with minimal difference between T_{50}(V) and T_{50}(Sr) (*33*). It is, however, noteworthy that the sticking coefficients of V and Sr species during evaporation/condensation under nebular conditions may not be identical such that differences in the volatilities of these two elements may not strictly reflect

differences in their T_{50}. Laboratory investigations of the fractionation factors of V and Sr species during free evaporation from CAI-like materials are required to further our understanding of the conditions and kinetics of evaporation processes that produced the δ^{51}V-δ^{88}Sr correlation observed in CAIs.

Last, we note that the lightest CAI composition on the δ^{51}V-δ^{88}Sr CAI correlation (CAI03) would require condensation of ~93 and ~89% of nebular V and Sr, respectively, in good agreement with Ca and Ti isotope systematics in CAIs requiring condensation of at least 85% Ca and 86% Ti (*30*). Likewise, accounting for the heaviest data point of this correlation (CAI75) through partial evaporation of a condensate taken as the lightest measured data point (CAI03) would require ~35% of the Sr and ~30% of the V to have been lost to the gas phase. These values are consistent with the ~10, ~28, and 15 to 50% evaporation of Ca, Ti, and Fe, respectively, required to account for isotope variations observed in CAIs (*30*, *32*), although lower evaporative losses would be expected for more refractory elements like Ca and Ti.

REE patterns

REE patterns of CAIs are indicative of their condensation and evaporation histories (*36*). All the fine-grained CAIs analyzed here have group II REE patterns, whereas coarse-grained CAIs have group I, V, or III REE patterns (fig. S2). The group II pattern is characterized by depletion in both the most refractory and the most volatile REEs (*36*). This signature is most consistent with a two-stage evaporation-condensation scenario of (i) closed-system, kinetically controlled evaporation of nebular dust, followed by (ii) vapor-solid separation, i.e., removal of an earlier ultrarefractory-REE host phase (e.g., hibonite), and condensation of the residual vapor (*60*, *61*). Although Sossi *et al.* (*21*) also observed δ^{51}V values close to bulk chondrites in coarse-grained CAIs and negative δ^{51}V values in fine-grained CAIs, they ruled out the possibility of a kinetic control on the observed variations of V isotopes based on the associated REE patterns. They argued that the observed group II REE patterns of fine-grained CAIs displaying negative δ^{51}V values provide evidence for their formation under equilibrium conditions from a gas previously depleted in the most refractory REE, "rendering kinetic vanadium isotopic fractionation untenable" (*21*). However, it has been demonstrated that mass-dependent isotopic variations of Ca (*29*, *62*, *63*), Ti (*30*), and Mg and Fe (*32*), the last two being particularly relevant here as they have 50% condensation temperatures roughly similar to V and Sr, are actually coupled with group II REE patterns. In detail, refractory inclusions with group II REE patterns tend to have lighter isotope compositions compared to those with group I REE patterns, implying kinetically controlled volatility fractionation during condensation of CAIs with group II REE patterns, after isolation of the ultrarefractory phase via partial evaporation (*30*, *61*). In light of the arguments presented here for the observed δ^{51}V-δ^{88}Sr correlation originating from kinetic isotope fractionation during evaporation and condensation, we suggest that light V isotope signatures associated with group II patterns in this study and Sossi *et al.* (*21*) are also most consistent with kinetic fractionation of V isotopes during condensation.

Coarse-grained CAIs investigated here have flat chondrite-normalized REE abundances (group I, V), except for notable depletions in the two most volatile REEs europium (Eu) and ytterbium (Yb) for three of five CAIs (group III; fig. S2). The group I, V REE patterns are most compatible with nearly complete condensation from a gas of nebular composition (*30*). Although CAIs with flat REE patterns tend not to have Ti mass fractionation effects (*30*), likely because Ti and REE condensed completely, or nearly so, into CAIs, V and Sr are less refractory than Ti [T_{50} ~ 1582 K; (*33*)] and so complete condensation of Ti does not imply complete condensation of V and Sr. This conclusion is supported by the fact that CAIs with flat REE patterns also have mass fractionation effects associated with evaporation events for elements with condensation temperatures close to V and Sr [e.g., Ni, Mg, and Fe; (*28*, *32*)]. Depletions in the most volatile elements in the group III pattern can be produced either in the case where the condensate was isolated from the gas before condensation of the more volatile elements or by distillation, whereby a CAI with a chondritic pattern is heated until the more volatile elements are evaporated. We favor this second scenario for the two coarse-grained CAIs 3529 and 75, for which the V-Sr isotope compositions are heavier than the chondritic composition and therefore inevitably require partial evaporation. Overall, the mass-dependent isotope compositions of our CAIs (i.e., V and Sr) are consistent with expectations from their REE patterns, both likely reflecting the fact that these samples or their precursor materials experienced multiple thermal events associated with kinetically controlled volatility fractionation.

Evaporation/condensation histories of CAIs

The approach adopted here to reproduce the V-Sr isotope composition of fine- and coarse-grained CAIs relies on a simplifying assumption that a single set of evaporation/condensation conditions can be used to explain the entire δ^{51}V-δ^{88}Sr trend. This assumption may, however, be at odds with the suggestion that the physicochemical conditions of evaporation/condensation were different between fine-grained CAIs (which basically are partial condensates) and coarse-grained CAIs (which have undergone melting and evaporation). For instance, notable W and Mo depletions in coarse-grained CAIs (mainly group I) have been used to argue that the oxygen fugacity during evaporation could have been markedly higher than that of the protosolar nebula (*58*). This indicates that the nature of the stable gas species of V and Sr could have differed during the condensation/evaporation processes involved in the formation of CAIs, therefore precluding the use of a single fractionation factor. Potential differences in the local conditions [e.g., partial pressure of the V and Sr gas species and surface properties of the solid (condensation) or liquid (evaporation)] could further complicate the description of the kinetic processes invoked here. However, the observation that all coarse-grained CAIs (groups III and I, V) and one fine-grained CAI (group II) fall on a single correlation line (Fig. 1) suggests that despite potential variations in the physicochemical conditions of the gas phase (including oxygen fugacity), the dominant stable gas species of V and Sr remained roughly constant over the entire condensation/evaporation history of CAIs. A fundamental expectation from partial evaporation/condensation is that the δ^{51}V should covary with V concentration, which, as already noted by Sossi *et al.* (*21*), is not observed in coarse-grained or fine-grained CAIs (Supplementary Materials). This could potentially imply that the CAIs did not initially originate from a homogeneous reservoir with respect to V. An alternative explanation is that V concentrations greatly vary across different CAI minerals such that different fragments of the same CAI (primarily coarse-grained) may exhibit variable bulk V concentrations depending on their dominant mineralogy. Future investigations of the distribution of V in different mineral

assemblages of CAIs have the potential to tackle this question and potentially document the extent of V heterogeneity in the CAI-forming region(s) of the PPD.

Additional CAI data may ultimately reveal the existence of different slopes in the observed δ^{51}V-δ^{88}Sr correlation, which are not resolvable at the present level of precision and/or with the available data. For instance, we cannot exclude the possibility that fine-grained CAI03 plots on a distinct δ^{51}V-δ^{88}Sr correlation line than coarse-grained CAIs (Fig. 5); if we define the δ^{51}V-δ^{88}Sr correlation using only the coarse-grained CAIs, then the correlation line narrowly fails to match the composition of CAI03. This therefore leaves the possibility for all group II CAIs (i.e., CAI01, CAI02, and CAI03) to have had an initial (i.e., before δ^{88}Sr disruption by aqueous alteration processes) δ^{51}V-δ^{88}Sr composition that did not plot on the exact same δ^{51}V-δ^{88}Sr correlation as non–group II CAIs. Such a possibility could reflect the fact that group II and non–group II CAIs experienced distinct evaporation-condensation histories (*60*, *61*), with group II CAIs having condensed from a gas already fractionated by condensation of perovskite ± hibonite (*37*). In this framework, it is likely that the correlation line through coarse-grained CAIs (Fig. 5) mainly reflects kinetic isotope fractionation during evaporation. More data are, however, required to test such hypothesis. Future investigations of δ^{51}V-δ^{88}Sr systematics in CAIs have the potential to further constrain (i) the proportions and relative volatilities of the dominant stable gas species of V and Sr in the protosolar nebula, as well as (ii) potential differences between the condensation/evaporation histories of group II (fine-grained) and non–group II (coarse-grained) CAIs. However, the fact that they all plot on a single correlation line invariably indicates that negligible, if any, δ^{51}V variability could have been generated by irradiation processes. For the rest of the discussion, we note that excluding CAI03 from the correlation line would make the maximum effect of ^{50}V production by irradiation processes even smaller (~0.07‰) than considered here (~0.2‰), therefore further strengthening our conclusion that in situ irradiation of coarse-grained CV CAIs by SCR was extremely limited or nonexistent.

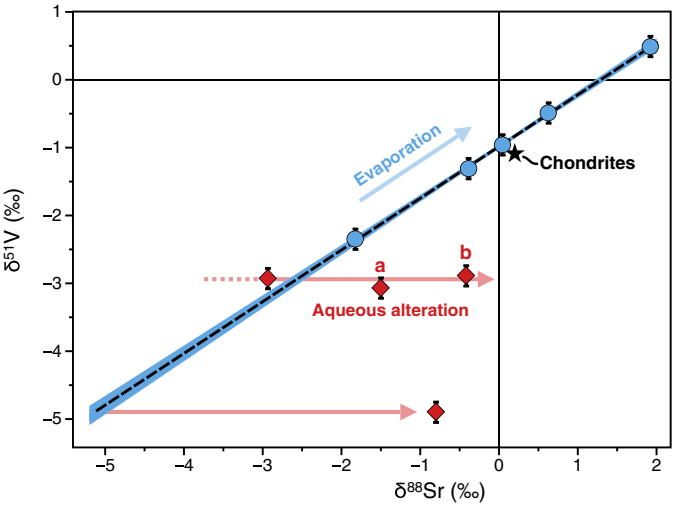

Fig. 5. δ^{51}V and δ^{88}Sr isotopic composition of fine- and coarse-grained CAIs (represented by red diamonds and blue circles, respectively). The black dashed line and its blue envelope represent the best fit and associated 95% CI, respectively, of the linear regression through all coarse-grained CAIs [$\delta^{51}V = (-0.9835 \pm 0.026) + (0.7623 \pm 0.022) \times \delta^{88}Sr$, $R^2 = 0.999$]. The chondritic composition (*34*, *40*, *41*) is indicated by the black star for reference. The two samples labeled "a" and "b" represent two fragments of the fine-grained CAI01. Errors are given as 2σ. The blue line represents the possibility that the correlation line through coarse-grained CAIs is mainly controlled by kinetic isotope fractionation during evaporation. In the framework of our model, most of the fine-grained CAIs are displaced toward higher δ^{88}Sr values due to partial equilibration of the δ^{88}Sr with aqueous fluids of chondritic composition [i.e., δ^{88}Sr = 0.2‰; (*40*, *41*)].

^{10}Be-^{10}B systematics in CAIs

Anomalously high ^{10}Be/^{9}Be$_0$ in CV chondrite CAIs [on the order of ~7×10^{-3}; (*21*) and this study] appear to be systematically computed from ^{10}Be-^{10}B isochrons associated with high MSWD values and very limited ranges of ^{9}Be/^{11}B [only up to ^{9}Be/^{11}B = 1.5 and 0.23 for Sossi *et al.* (*21*) and this study, respectively]. This implies that the exact levels of ^{10}Be in these samples are difficult to quantify with confidence (*38*). Given that Be [T_{50} = 1452 K (*33*)] is much more refractory than B [T_{50} = 908 K (*33*)), such low ^{9}Be/^{11}B values [corresponding to B concentrations >200 ng/g (*21*)] are unlikely to reflect the pristine composition of CAIs and would most likely reflect sample contamination by B of secondary origin. This contamination could potentially occur (i) on the meteorite parent body by mobilization of B from the chondritic matrix into the CAI during parent body aqueous alteration, (ii) during terrestrial weathering, and/or (iii) during sample preparation, such as cutting or polishing. The slope of an isochron defined over a restricted range of ^{9}Be/^{11}B values becomes particularly sensitive to the ^{10}B/^{11}B ratio of the analysis with the lowest ^{9}Be/^{11}B, which can be analyzed with the highest precision. In many cases, sample contamination by B of secondary origin would cause the slope of the associated isochrons to increase, given that the initial ^{10}B/^{11}B of CAIs often are higher than both bulk chondrite and terrestrial B, hence leading to overestimations of ^{10}Be/^{9}Be$_0$ (*38*). Dunham *et al.* (*38*) also pointed out that cosmic ray interaction with meteorite parent bodies can induce spallation of O nuclei, resulting in the production of cosmogenic B, which would further increase the slope of ^{10}Be-^{10}B isochrons and therefore represent another potential source of ^{10}Be/^{9}Be$_0$ overestimation. However, all the aforementioned processes will be essentially muted for isochrons that include large ranges of ^{9}Be/^{11}B, which is consistent with the essentially invariant ^{10}Be/^{9}Be$_0$ (~8×10^{-4} within uncertainty; fig. S10) found in CV chondrite CAIs with high ^{9}Be/^{11}B and statistically significant ^{10}Be-^{10}B isochrons [e.g., (*5*–*10*, *13*)]. It is worth noting that ^{10}Be/^{9}Be$_0$ values ranging from normal CV3 CAI-like ratios up to $(104 \pm 16) \times 10^{-4}$ have been suggested for CAIs from CB/CH chondrites, with ^{9}Be/^{11}B ≥ 10 (*64*, *65*). On the basis of the observation that, irrespective of their $(^{10}Be/^{9}Be)_0$ values, CH/CB chondrite CAIs invariably display chondritic-like Li isotope ratios, Fukuda *et al.* (*65*) argued that ^{10}Be excesses in CH/CB chondrite CAIs are most compatible with irradiation of nebular gas before CAI condensation. However, these isochrons remain associated with high MSWD (*38*), which renders quantification of the corresponding ^{10}Be excesses uncertain. Recently, Fukuda *et al.* (*66*) found ^{10}Be/^{9}Be$_0$ up to $(29 \pm 6) \times 10^{-4}$ (max ^{9}Be/^{11}B ~ 300) for melilite grains in CO chondrite CAIs with canonical $(^{26}Al/^{27}Al)_0$. The authors suggest that higher ^{10}Be/^{9}Be$_0$ in CO CAIs relative to CV CAIs could reflect a heterogeneous distribution of ^{10}Be in the nascent Solar System, with CO CAIs having potentially formed closer to the Sun (where ^{10}Be was produced more efficiently) than CV CAIs. Understanding the origin and distribution of ^{10}Be in the early Solar System and

establishing whether or not CV CAIs can be considered as representative of the entire CAI population will require additional investigation of Be-B systematics of CAIs from various types of chondrites.

V isotope constraints on CAI records of solar irradiation

Here, we use the V isotopic composition of CAIs together with their initial ^{10}Be abundances to quantify irradiation conditions in the early Solar System, in light of our assertion that V isotopes in CAIs record no detectable evidence of irradiation. We model the irradiative production of ^{10}Be and ^{50}V using the thin target approximation, whereby the number of atoms of any isotope produced by irradiation depends on three unknown parameters: (i) the concentration of the target nuclei (i.e., the chemical composition for the target material), (ii) the spectral slope (p), which quantifies the relative abundance of high- and low-energy protons [low-p and high-p events corresponding to gradual (p ~ 2.7) and impulsive (p ~ 3.5) flares, respectively (*3*, *20*)], and (iii) the total fluence above 10 MeV experienced by the target (F_{10}) [e.g., (*21*)]. Cross sections for reactions of ^{10}Be and ^{50}V production by irradiation in the early Solar System (Supplementary Materials) were taken from Sisterson *et al.* (*67*) and calculated using the TALYS code (*68*), respectively, before being implemented into a Matlab code based on Liu and McKeegan (*69*) and Liu *et al.* (*70*).

At a given p value (which hence indicates the type of flare), expected ^{50}V anomalies and ^{10}Be/^{9}Be$_0$ values increase together as a function of F_{10}. Because of energy loss when charged particles penetrated the gas phase of the PPD, the total particle flux decreases and the energy spectrum becomes shallower with increasing heliocentric distance. To evaluate the maximum degree of cosmogenic ^{50}V production that could be produced by in situ irradiation, we assume no energy loss (i.e., no "stopping"), which equals to considering the full irradiation power from the proto-Sun. If stopping were considered, then the extent of V isotope anomaly produced by CAI irradiation should be even smaller than considered here, therefore reinforcing our conclusions. We also note that the flux of energetic protons from the proto-Sun—here taken from Gounelle *et al.* (*3*) and Lee *et al.* (*20*), who considered the x-ray luminosity emitted from a solar mass protostar—is associated with a large systematic uncertainty. Because the flux of energetic protons and time of irradiation together control the modeled dose of irradiation seen by CAIs, inherent uncertainties associated with particle flux estimates may imply that quantitative constraints on the dose and duration of CAI irradiation may not be taken at face value. Nonetheless, because our work builds upon previous work from Gounelle *et al.* (*3*), Lee *et al.* (*20*), and Sossi *et al.* (*21*), direct comparison of our results with outcomes from these previous studies is, however, justified.

Previously, Gounelle *et al.* (*3*) demonstrated that irradiation of proto-CAIs (all considered to have similar target abundances) in the framework of the X-wind model should produce ^{50}V enrichments corresponding to δ^{51}V = −3.4 to −7.1‰, with a best-estimate prediction of −4.5‰. In Sossi *et al.* (*21*), different combinations of p and F_{10} values were required to explain V isotope anomalies across CAIs that yet pertained to the same ^{10}Be-^{10}B isochron. Here, we compute the expected V isotopic compositions and initial ^{10}Be abundances of CAIs that are irradiated by gradual (p = 2.7) or impulsive (p = 3.5) flares at variable distances from the proto-Sun (0.02, 0.1, 0.5, and 1 AU). The relative abundances of target elements for the irradiative production of ^{10}Be (^{16}O) and ^{50}V (^{50}Ti, ^{52}Cr, ^{48}Ti, ^{49}Ti, ^{50}Ti, and ^{51}V) are adjusted by considering either (i) a proto-CAI in situ irradiation scenario, where we take the chemical compositions of the CAIs analyzed in this study, or (ii) a solar gas irradiation scenario, where we consider the bulk composition of CI chondrites to be representative of the nebular gas abundances. Iron (specifically ^{56}Fe) represents a potentially important (*34*, *49*) and previously overlooked (*21*) target for the production of V. One difficulty here is, however, that a substantial fraction of the Fe now present in CAIs is of secondary origin, and so, the present-day concentrations of Fe cannot be used to model the irradiative production of V isotopes in CAIs. For conservative purposes, we consider ^{50}V production from ^{56}Fe only for the solar gas irradiation scenario, which means that CAI irradiation calculations represent minimum predicted V isotope anomalies.

First, we compute the expected durations of irradiation and V isotope compositions of proto-CAIs, assuming that all of their excess ^{10}Be originates from in situ irradiation at ~0.1 AU in the PPD. V isotope variations are expressed as $\Delta^{51}V = \delta^{51}V - \delta^{51}V_{init}$ (‰), corresponding to δ^{51}V deviations relative to its starting composition ($\delta^{51}V_{init}$). We find that, depending on their chemical compositions, some CAIs require a threefold longer duration of irradiation than others to reach similar ^{10}Be/^{9}Be$_0$ ~ 8 × 10^{-4} (e.g., 900 years versus 300 years; Fig. 6). As a result, the homogeneous levels of ^{10}Be excess in CAIs would have to be coincidental. An alternative possibility could be that the Be isotope compositions of the coarse-grained CAIs were reset by exchange with the surrounding gas during the evaporation process that affected V isotopes. However, a selective re-equilibration of Be (and not V) isotopes is unlikely given the similar volatilities of these two elements (*33*). The fact that all six CAIs define a linear δ^{51}V-δ^{88}Sr correlation (within ±0.2‰

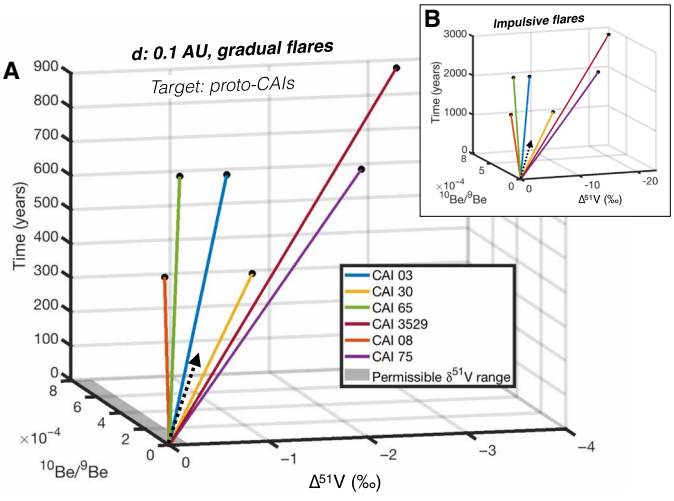

Fig. 6. Three-dimensional (3D) diagram of the trajectories of proto-CAIs, in ^{10}Be/^{9}Be, $\Delta^{51}V = \delta^{51}V - \delta^{51}V_{init}$ (‰), and time (years) space, in the case of in situ irradiation at 0.1 AU. Irradiation by gradual and impulsive flares is shown in panel (**A**) and panel (**B**), respectively. The difference trajectories of CAIs, which all reach the canonical ^{10}Be/^{9}Be of ~8 × 10^{-4} (black dots), are controlled by their distinct abundances of target elements for cosmogenic production (Supplementary Materials). Note that all of these six CAIs plot on the δ^{51}V versus δ^{88}Sr correlation line (Fig. 1). The permissible range of δ^{51}V variation (~0.2‰) is represented by the gray area. Dashed arrows show the general direction of 10Be and 50V irradiative production. 2D projections of (A) and (B) are provided in the Supplementary Materials to facilitate readability.

uncertainty) implies that irradiation processes can account for a maximum of 0.2 Δ^{51}V units throughout the condensation-evaporation history of each CAI. Our simulations, however, demonstrate that V isotope heterogeneities of at least 2‰ (here, we say "at least" as this ignores potential ^{50}V production with isotopes of Fe as a target) should be generated to reach ^{10}Be/^{9}Be$_0$ ~ 8×10^{-4} via in situ irradiation of proto-CAIs by gradual flares (Fig. 6). In line with previous findings (*3*, *21*), these anomalies would be even greater (~10‰) in the case of impulsive flares (Fig. 6). Accounting for ^{10}Be abundances in CAIs by in situ irradiation therefore results in large discrepancies between the observed and calculated V isotope compositions of the proto-CAIs. Together, these observations firmly rule out in situ irradiation of proto-CAIs at the inner edge of the PPD as a likely origin for ^{10}Be excesses in CV CAIs.

The homogeneous levels of ^{10}Be excess associated with statistically meaningful ^{10}Be-^{10}B isochrons in CV CAIs (*38*) could potentially be consistent with CAIs condensing from nebular gas that had been previously enriched in ^{10}Be [and other short-lived radionuclides such as ^{26}Al, ^{41}Ca, and ^{53}Mn (*71*)] via SCR irradiation (*13*). This process of ^{10}Be production at the surface of the PPD could have taken place at disk radii >0.1 AU and up to 1 AU (*72*), suggesting that CAI formation could have occurred at much greater distances than previously considered. Here, we compute the maximum ^{10}Be excesses that could have been produced by irradiation of nebular gas without generating Δ^{51}V greater than 0.2‰ (Fig. 7). We find that this V isotope constraint would systematically require ^{10}Be-^{10}B$_0 \leq 1 \times 10^{-4}$, which is about one order of magnitude lower than observed in CAIs. Unlike for the scenario of in situ irradiation, there is a possibility here that all CAIs found today in meteorites inherited homogeneous levels of ^{10}Be excess during condensation. We therefore also computed the expected V isotope compositions of CAIs, assuming that all of their excess ^{10}Be originates from irradiation of nebular gas before their condensation. Our results show that generating ^{10}Be/^{9}Be$_0$ ~ 8×10^{-4} by SCR irradiation of nebular gas would produce δ^{51}V about 1.5‰ and 4.0‰ lighter than the starting composition of the gas, for gradual and impulsive flares, respectively, on time scales that mainly depend on the heliocentric distance of the irradiation (Fig. 7). Hence, according to this scenario, the starting V isotope composition of proto-CAIs should have been lighter than the chondritic value by at least 1.5‰ (considering gradual flares). While this would slightly modify the linear functions presented in Table 1 [e.g., the $f(\mathrm{V}) - f(\mathrm{Sr})$ relationship for V and Sr during condensation would become $f(\mathrm{V}) = 0.7246 \times f(\mathrm{Sr}) + 0.2757$], this scenario cannot be ruled out as long as all proto-CAIs inherit identical ^{10}Be and ^{50}V anomalies upon formation. This may require efficient mixing and homogenization of the nebular gas by turbulent diffusion and gravitational instabilities, which both can rapidly homogenize short-lived radionuclides within disks on time scales of less than 10^5 years [e.g., (*73*)], comparable to the time scales required for ^{10}Be production in the nebular gas at ~1 AU (Fig. 7B).

The observation of homogeneous levels of ^{10}Be excess (*38*) is also potentially consistent with an interstellar origin of ^{10}Be in CAIs, which could have been produced via interaction between energetic protons of GCRs and C-N-O nuclei (*11*, *12*). CAIs with fractionation and unidentified nuclear effects (FUN CAIs) appear to have initially contained ^{10}Be/^{9}Be at the level of (3 to 5) $\times 10^{-4}$ [e.g., (*7*, *9*, *70*)], similar to the inferred ^{10}Be/^{9}Be$_0$ of $(5.1 \pm 1.4) \times 10^{-4}$ in ^{26}Al-free platy hibonite crystals (PLACs) (*74*, *75*). Potentially higher ^{10}Be/^{9}Be$_0$ in canonical CV3 CAIs (~8×10^{-4}) could potentially reflect the addition of protosolar nebula spallogenesis to a baseline level inherited from the protosolar molecular cloud and best represented by FUN CAIs (*9*, *12*, *70*). This scenario may be in line with models of ^{10}Be production by nebular gas irradiation by SCRs at the surface of the PPD, which predict that the ^{10}Be/^{9}Be of the gas phase at the CAI condensation front would increase with time, hence potentially explaining the reduced values in presumably early (before ^{26}Al injection) generations of CAIs relative to later (after ^{26}Al injection) generations (*72*).

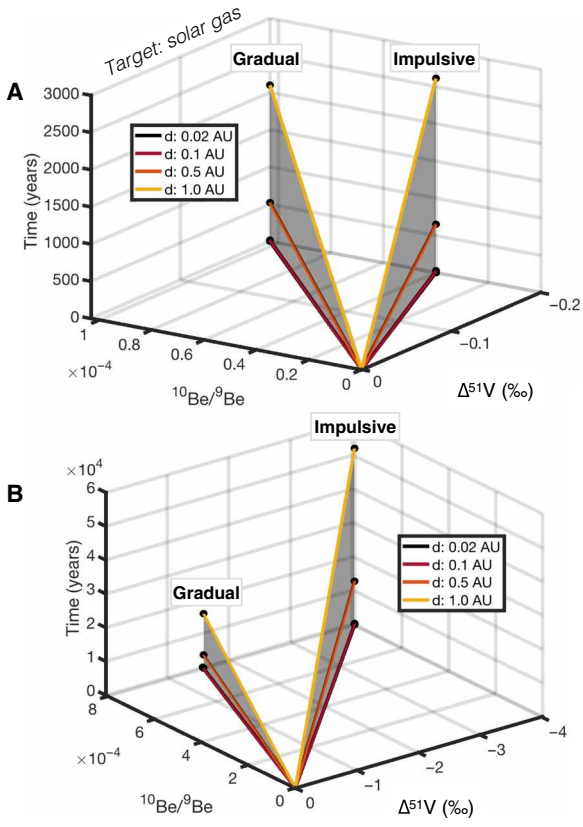

Fig. 7. 3D diagram of the trajectories of nebular gas composition in ^{10}Be/^{9}Be, Δ^{51}V (‰), and time (years) space, in the case of irradiation at 0.02, 0.1, 0.5, and 1.0 AU by gradual and impulsive flares. (**A**) Expected ^{10}Be/^{9}Be variations associated with Δ^{51}V values of ~−0.2‰ (black dots). (**B**) Expected δ^{51}V variations associated with a canonical ^{10}Be/^{9}Be of ~8×10^{-4} (black dots). 2D projections of (A) and (B) are provided in the Supplementary Materials to facilitate readability.

Cosmolocation of the CAI factory

The vast majority of CAIs formed 4567.2 ± 0.2 Ma ago, over a period of ~40,000 to 200,000 years (*17*–*19*, *76*), possibly while the Sun was in transition from the protostellar into a pre–main sequence (T Tauri) phase of star formation (*77*). The ^{26}Al/^{27}Al systematics of bulk CAIs suggests that the formation of ^{26}Al-rich refractory inclusions was a punctuated and recurrent process, possibly associated with episodic flare-ups, in the form of FU-Orionis and EX-Lupi outbursts [e.g., (*61*, *78*, *79*)]. Larsen *et al.* (*80*) proposed that CV CAIs could have formed on the time scale of <8000 years via chemical processing of ^{26}Al-rich presolar carriers in a hot zone proximal to the proto-Sun (<0.1 AU). In analogy to the X-wind model for ^{10}Be and other short-lived radionuclides (*3*, *20*), proto-CAIs would then

be extracted from the inner edge of the disk and propelled above the disk's midplane by magnetocentrifugal outflows before raining back on the disk at chondrite-forming heliocentric distances [e.g., (*81*)]. Here, V isotope systematics offer a unique opportunity to test the likelihood of this model by bringing constraints on the maximum duration that proto-CAIs could have spent at the inner edge of the disk before generating V isotope anomalies that exceed the 0.2‰ maximum variability permitted by the δ^{51}V-δ^{88}Sr correlation (Fig. 1). On the basis of the concentrations of the target nuclei measured for each of the six CAIs plotting on the δ^{51}V-δ^{88}Sr correlation, we compute the evolution of V isotope compositions as a function of time for proto-CAIs at 0.02 or 0.1 AU in the case of gradual or impulsive flares (Fig. 8). We find that, in the case of gradual flares, 50 years is the maximum duration of exposure that these CAIs could have spent within 0.1 AU of the proto-Sun before V isotope heterogeneities greater than 0.2‰ should be observed among the CAIs analyzed in this study. Observations of the Orion nebula star cluster in the framework of the Chandra Orion Ultradeep Project suggest that YSOs may spend ~10 to 20% of their time in flare activity [e.g., (*1*)]. Taken at face value, these numbers suggest an upper limit of ~500 years for the residence time of each CAI at <0.1 AU from the proto-Sun, which is over one order of magnitude shorter than the lifetime of proto-CAIs as inferred from ^{26}Al/^{27}Al systematics (*80*). In other words, if CAIs formed <0.1 AU from the proto-Sun, then each individual CAI must have been transported very rapidly outward (i.e., within 500 years) after initial condensation, while at the same time more CAIs continued being formed in the CAI-forming region, within 0.1 AU.

Taking these considerations together with the absence of evidence for in situ irradiation of CAIs at the inner edge of the Solar System (as argued in this contribution), we propose that CAIs most likely formed at greater heliocentric distances in the PPD (>0.1 AU) during the early phases of molecular cloud infall and Solar System buildup. A growing number of observational and theoretical studies indicate that newborn PPDs form compact objects whereby presolar material infalling from the deeper envelopes of the parental molecular cloud is supplied close to the protostar and is readily vaporized (*26*, *82*–*84*). Concurrently with this injection, the disk expands outward by viscous spreading: the high-temperature nebular gas thus progressively cools down, allowing condensation to occur up to 1 to 2 AU from the proto-Sun (Fig. 9) (*26*, *47*, *84*). The fraction of CAIs that is hence transported to the outer Solar System and not accreted to the central star would decrease through time as the disk expands, with the earliest formed CAIs ultimately dominating the outermost regions of the PPD (*26*). Such a model, where the greater heliocentric distance of CAI formation limits the amount of time during which CAIs could have been exposed to inner Solar System irradiation (Fig. 9), appears consistent with the absence of detectable irradiation-related V isotope anomalies in CAIs. Furthermore, this scenario relaxes the need for a mechanism of strong outward transport of CAIs during the lifetime of the PPD (e.g., stellar outflows), which would essentially occur simultaneously with CAI formation itself. The formation of CAIs from a unique reservoir associated with the earliest stages of molecular cloud material infall is also consistent with the fact that oxygen isotope systematics are similar in inner and outer Solar System CAIs, indicating derivation from a common source reservoir in the early PPD evolution (*85*). Whether or not bipolar outflows propelled by disk—and not stellar—magnetic fields [e.g., (*86*)], which could potentially sample material from as far out as 1 AU, played a role in the outward transport of CAIs remains open to discussion. Models of CAI formation during FU- and EX-outbursts or similar events could allow CAI formation out to at least 1 AU [e.g., (*79*)].

Other records of irradiation in CAIs have been suggested in the literature. Weakly correlated variations of ^{9}Be/^{6}Li and ^{7}Li/^{6}Li in CV CAIs have, for instance, been proposed to reflect the in situ decay of cosmogenic ^{7}Be [$T_{1/2}$ = 53 days; (*8*, *87*)]. Whether or not potential ^{7}Li excesses in CAIs can be interpreted in terms of early Solar System irradiation has, however, been called into question due to the extremely short half-life of ^{7}Be and complex geochemical behavior of Li [e.g., (*88*)], and the question still remains open to debate. Cosmogenic noble gases in CAIs constitute another potential tracer of in situ irradiation (i.e., no inheritance from the time of condensation). Helium and neon excesses recently measured in PLACs were interpreted to record low temperature irradiation at a considerable distance from the proto-Sun (*89*), which appears consistent with the early transport of CAIs to the outer Solar System and their limited exposure to irradiation conditions prevailing at the inner edge of the PPD. Proton fluences required to produce the observed cosmogenic noble gas abundances in PLACs were deemed insufficient to explain the corresponding ^{10}Be/^{9}Be ratios, further indicating that part of ^{10}Be in CV CAIs was generated before their

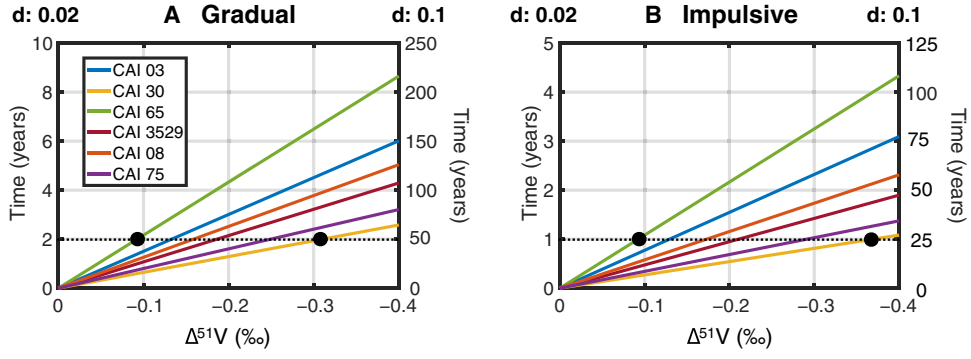

Fig. 8. Trajectories of proto-CAI compositions in time (years) versus Δ^{51}V (‰) space, in the case of in situ irradiation at 0.02 AU or 0.1 AU. Irradiation by gradual and impulsive flares is shown in panel (**A**) and panel (**B**), respectively. This demonstrates that V isotope heterogeneities greater than 0.2‰ should be observed in CAIs analyzed in this study after ≤50 years and ≤25 years in the case of gradual and impulsive flares, respectively, hence placing strong constraints on the maximum duration (~500 years; see main text) that CAIs could have remained at the inner edge of the Solar System in the framework of in situ irradiation model [e.g., (*21*)].

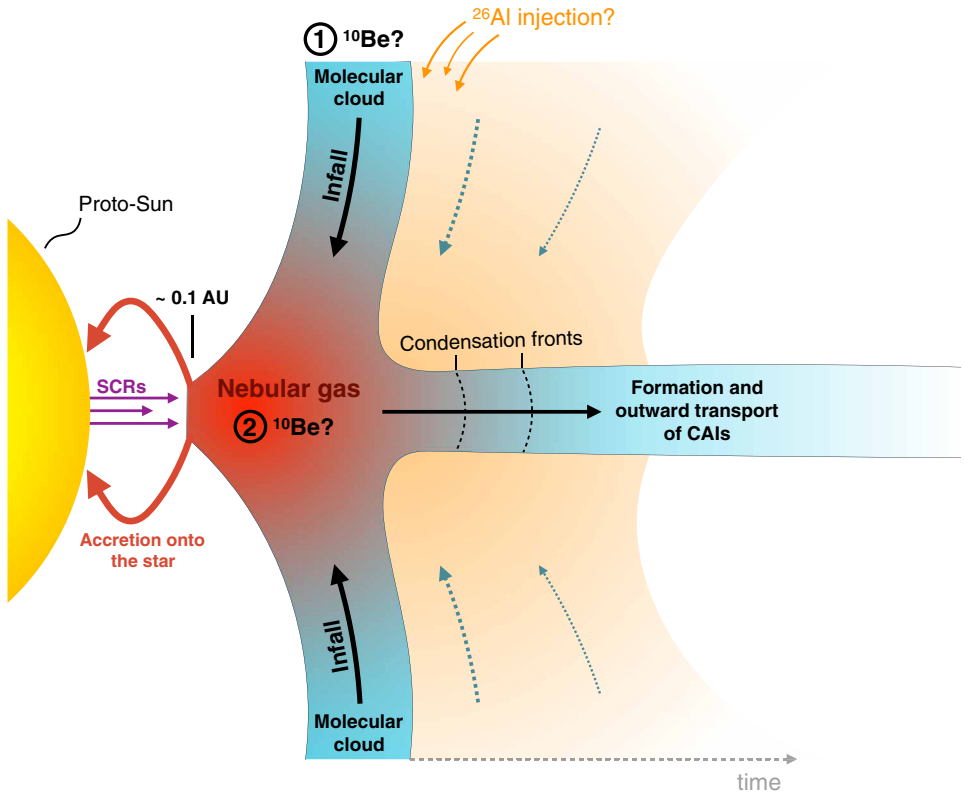

Fig. 9. Schematic model of CAI formation location in the PPD consistent with current models proposed for the early dynamical (*26*, *82*), chemical (*84*), and isotopic (*47*) evolution of the PPD (not to scale). Infalling material from the parental molecular cloud is readily vaporized in the inner PPD, producing a gas phase that is directly exposed to SCRs from the young Sun. The earliest CAIs, formed by cooling of the gas during its outward viscous spreading, are readily transported to the outer edge of the PPD with limited exposure to inner Solar System conditions. According to our numerical simulations, the two possible scenarios for the origin of ^{10}Be excess in CAIs correspond to (1) inheritance from the interstellar medium (*11*, *12*) and (2) irradiation of the nebular gas before CAI formation (*13*).

in situ exposure to solar particles (*89*). However, whether or not CV CAIs can be considered as representative of the entire CAI population remains to be seen. To this extent, combining V-Sr isotope and Be-B systematics in CAIs from various types of chondrites constitutes a promising avenue to further constrain fossil records of in situ irradiation in meteorites [e.g., ^{10}Be excesses relative to CV CAIs (*64*–*66*)] and elucidate on the origin and distribution of ^{10}Be in the early Solar System.

MATERIALS AND METHODS

V and Sr isotope measurements

Splits of 5 to 15 mg of CAI fragments for V and Sr isotope analyses (CAIs 08, 30, 65, 75, and 3529) were handpicked under a binocular microscope where great care was taken to select the most pristine fragments and avoid including matrix material. After handpicking, fragments were directly digested without powdering using double-distilled concentrated HF, HNO_3, and HCl. Insoluble phases (fluorides and refractory minerals like spinel) were further digested in concentrated nitric acid in an Anton Parr high-pressure asher at ~110 bar and 260°C. All samples were fully digested using the above-described method with no solid residue remaining. Vanadium was separated from the sample matrix using a four-step cation/anion exchange chromatography procedure described in detail elsewhere (*48*, *92*). Briefly, the method comprises one cation exchange resin column in 1 M HNO_3, followed by three anion exchange resin columns where V is bound to the resin by complexation with H_2O_2 (*92*). Throughout the study, chemical yields were >90% by comparing the amount of V initially loaded onto the first column with the amount recovered for isotope measurement. We furthermore monitored losses of V with an iCAP ICPMS (inductively coupled plasma mass spectrometer) instrument by checking that column eluents did not contain any significant V (<1% of V loaded). Blanks were monitored with each batch of samples and were always <2 ng, which is insignificant compared with the >1000-ng V processed for each sample.

Vanadium isotope ratios were measured using a Neptune multiple-collector ICPMS, located at the Plasma Mass Spectrometry Facility of the Woods Hole Oceanographic Institution (WHOI). Isotope compositions were determined using standard sample bracketing with the Alfa Aesar reference solution that is defined as $\delta^{51}V = 0‰$ (*92*). Each unknown sample was interspersed with a pure V reference solution from BDH Chemicals that has now been measured in nine separate studies with the indistinguishable $\delta^{51}V = -1.18 \pm 0.02‰$ (2SE) (*21*, *34*, *48*, *92*–*97*). The mass spectrometer was operated in medium resolution mode. To quantify and correct for isobaric interferences of ^{50}Ti and ^{50}Cr on ^{50}V, the masses ^{48}Ti, ^{49}Ti, ^{52}Cr, and ^{53}Cr were monitored and a mass bias correction routine using ^{49}Ti/^{50}Ti and ^{53}Cr/^{50}Cr ratios was applied (*93*, *98*). Mass ^{51}V was collected using a Faraday cup equipped with a 10^{10} ohm resistor, whereas Faraday cups with conventional 10^{11} ohm resistors were

used to collect all other masses. Samples and standards were measured at a concentration of 800 ng/ml V, which produced an ion beam of ~2 nA on ^{51}V and ~0.005 nA on ^{50}V. Precision and accuracy of the V isotope measurements were assessed by measuring the BDH standard throughout the study (covering the period from April 2018 to January 2019) and by processing U.S. Geological Survey (USGS) reference materials AGV-2, BHVO-2, and BCR-2 with every batch of unknown samples. These reference materials have previously been analyzed by different laboratories (*48*). The resulting mean $\delta^{51}V$ values for AGV-2, BHVO-2, and BCR-2 for the analytical period of the CAI measurements were −0.79 ± 0.12‰ (2SD; n = 11), −0.87 ± 0.14‰ (2SD; n = 4), and −0.81 ± 0.08‰ (2SD; n = 10), respectively, which is in excellent agreement with previous studies (*43*, *48*, *93*, *99*, *100*). These external errors are similar to those obtained for the CAIs here, which exhibit 2SD ranging from 0.06 to 0.24‰ (table S2).

Elemental concentrations were determined for a subset of the samples using a ThermoFinnigan iCAP quadrupole ICPMS, located at the WHOI Plasma Mass Spectrometry Facility. Concentrations were calculated via reference to ion beam intensities obtained from a five-point calibration curve constructed from serial dilutions of a gravimetrically prepared multi-element standard; drift was monitored and corrected via normalization to indium intensities. Accuracy and precision were better than ±7% (2SE) based on the correspondence of concentrations in USGS reference materials AGV-2, BCR-2, and BHVO-2 determined during the same analytical sessions as the CAIs.

Strontium separation and mass spectrometry closely follows the methods outlined by Charlier *et al.* (*101*). In brief, each sample was separated in two aliquots, one of which was optimally spiked with ^{84}Sr-^{87}Sr double-spike and the other left unspiked. From this point, the double-spike and natural aliquots were processed independently. For radiogenic Sr measurements in CAIs 01, 02, and 03, this corresponds to 33.2, 5.8, and 23 mg, respectively, and to 10, 4.3, and 15.5 mg, respectively, for double-spike measurements. Separation of Sr was undertaken using custom-made 2-ml Teflon columns and Sr spec resin closely following the procedure outlined by Deniel and Pin (*102*). Column yields were consistently high, 90% or higher. Purified Sr fractions were loaded onto outgassed Re filaments along with a TaF_5 activator ready for analysis by thermal ionization mass spectrometry (TIMS) with a Thermo Scientific TRITON at the University of Durham. The interference of ^{87}Rb on ^{87}Sr is corrected for using measured ^{85}Sr signals and assuming a ratio of $^{87}Rb/^{85}Rb = 0.385041$.

Fractionation induced by the column is taken into account with the instrumental mass fractionation during the deconvolution of both spiked and natural (unspiked) measurements and solved in ^{87}Sr denominator space using a Newton-Raphson iterative technique (*103*). The average value of the international Sr carbonate standard NBS 987 over the course of this study was $^{87}Sr/^{86}Sr = 0.7102385 \pm 0.0000068$ [2SD; n = 26; ±9.5 parts per million (ppm)]. Independent dissolutions and measurements of the USGS rock standard BHVO-1 basalt yield an average of $\delta^{88}Sr = 0.268 \pm 0.009$‰ (2 SD; n = 5), which equates to an external precision of ±9.5 ppm. Total procedural blanks were routinely less than 20 pg, which is negligible (<0.02%) for all the samples analyzed here.

Be-B measurements

Boron isotope ratios were determined by SIMS using a Cameca ims1280 ion microprobe at the North-Eastern National Ion Microprobe Facility at the WHOI in two sessions in January and February 2016, following the method described by Marschall and Monteleone (*104*). Yet, the analytical details are, in part, repeated and specified here in some detail, because the ranges of B concentration of the CAI minerals investigated here (~0.26 to 120 ng/g) are one to three orders of magnitude lower than those in the Mid-Ocean Ridge Basalt glasses described in that study (~400 to 2500 ng/g). Also, the setup used here for the CAI minerals included the analysis ^{9}Be. The parameters for B isotope analyses were as follows: 40-nA, 22-keV ^{16}O primary ion beam; 10-kV secondary acceleration voltage; ±40-eV energy window without offset; and secondary ion detection by a single-electron multiplier in counting mode (electronically set dead time τ = 28 ns).

A 75 μm × 75 μm raster was applied during presputtering to remove the gold layer and to reduce surface contamination. Presputtering lasted for 300 s. Before each measurement, mass calibration of $^{9}Be^{+}$, $^{10}B^{+}$, and $^{11}B^{+}$ was performed, and fine-tuning of the secondary column deflectors, stigmators, and lenses was done manually to maximize the signal of $^{28}Si^{2+}$ (except for spinel) on the electron multiplier, thereby maintaining maximum transmission throughout the session. A 2000 μm × 2000 μm field aperture was used to exclude the edge of the secondary beam, again reducing the influence of surface contamination (*104*, *105*). The analyses were performed using a rastered area of 50 μm × 50 μm in the center of the larger presputtered area.

Forty cycles were measured per analysis for the reference glasses. One hundred cycles were measured in most sample analyses, except where boron contents were high and the number of cycles was reduced to 40 to 84. On one spot, 248 cycles were measured to evaluate possible down-hole analytical drift, which was found to be insignificant. During each cycle, masses were switched between $^{9}Be^{+}$, $^{10}B^{+}$, and $^{11}B^{+}$. The integration times per cycle were 3.04, 20, and 10 s, respectively. The mass resolution $m/\Delta m$ was set to ~1250 at 10% intensity ratio, which is sufficient to remove possible molecular interferences [e.g., (*106*)]. The total time required for one 100-cycle analysis was 55 min. The raw count rates were corrected for both the multiplier deadtime and for the slow changes in secondary ion intensity over the course of a single measurement (i.e., time interpolation). The latter was done by averaging respective counts of ^{9}Be and ^{10}B from two subsequent cycles and calculating the $^{9}Be/^{11}B$ and $^{10}B/^{11}B$ ratios by dividing the count rates of the intermediate ^{11}B measurement by that average. Each analysis consisting of n analytical cycles, therefore, produced $n - 1$ isotope ratios. The count rates were also corrected for the machine background of 0.086 s^{-1}, which was determined by analyzing mass 9.7 on silica glass Hersasil-102 with a total integration time of 91 min. This correction is important for CAI minerals, where the background-corrected count rates for ^{10}B (the isotope with the lowest count rate) were between 0.24 and 46 s^{-1} (0.26 to 120 ng/g B).

Last, the $n - 1$ calculated isotope ratios of each analysis were filtered for statistical outliers >3σ. Isotope ratios calculated from averaging a number of ratios collected over the course of a single analysis are positively biased, if the arithmetic mean of the count rate ratios is taken (*107*). This bias was avoided in this study by using the geometric mean of the $n - 1$ isotope ratios (note that the geometric SD is always smaller than the arithmetic SD). Beryllium and B concentrations were estimated from $^{9}Be^{+}$ and $^{11}B^{+}$ count rates relative to the respective count rates during analysis of the glass reference materials corrected for the relative intensities of the

primary beam. Additional details about our analytical procedure are presented in the Supplementary Materials.

SUPPLEMENTARY MATERIALS

Supplementary material for this article is available at https://science.org/doi/10.1126/sciadv.abg8329

REFERENCES AND NOTES

1. S. J. Wolk, F. R. Harnden Jr., E. Flaccomio, G. Micela, F. Favata, H. Shang, E. D. Feigelson, Stellar activity on the young suns of Orion: COUP observations of K5-7 pre-main-sequence stars. *Astrophys. J. Suppl. Ser.* **160**, 423–449 (2005).
2. C. Ceccarelli, C. Dominik, A. López-Sepulcre, M. Kama, M. Padovani, E. Caux, P. Caselli, HERSCHELFINDS evidence for stellar wind particles in a protostellar envelope: Is this what happened to the young sun? *Astrophys. J. Lett.* **790**, L1 (2014).
3. M. Gounelle, F. H. Shu, H. Shang, A. E. Glassgold, K. E. Rehm, T. Lee, Extinct radioactivities and protosolar cosmic rays: Self-shielding and light elements. *Astrophys. J.* **548**, 1051–1070 (2001).
4. J. Chmeleff, F. von Blanckenburg, K. Kossert, D. Jakob, Determination of the ^{10}Be half-life by multicollector ICP-MS and liquid scintillation counting. *Nucl. Instrum. Methods Phys. Res. Sect. B* **268**, 192–199 (2010).
5. K. D. McKeegan, M. Chaussidon, F. Robert, Incorporation of short-lived ^{10}Be in a calcium-aluminum-rich inclusion from the Allende meteorite. *Science* **289**, 1334–1337 (2000).
6. N. Sugiura, Y. Shuzou, A. Ulyanov, Beryllium-boron and aluminum-magnesium chronology of calcium-aluminum-rich inclusions in CV chondrites. *Meteorit. Planet. Sci.* **36**, 1397–1408 (2001).
7. G. J. MacPherson, G. R. Huss, A. M. Davis, Extinct ^{10}Be in type A calcium-aluminum-rich inclusions from CV chondrites. *Geochim. Cosmochim. Acta* **67**, 3165–3179 (2003).
8. M. Chaussidon, F. Robert, K. D. McKeegan, Li and B isotopic variations in an Allende CAI: Evidence for the in situ decay of short-lived ^{10}Be and for the possible presence of the short-lived nuclide ^{7}Be in the early solar system. *Geochim. Cosmochim. Acta* **70**, 224–245 (2006).
9. D. Wielandt, K. Nagashima, A. N. Krot, G. R. Huss, M. A. Ivanova, M. Bizzarro, Evidence for multiple sources of ^{10}Be in the early solar system. *Astrophys. J. Lett.* **748**, L25 (2012).
10. G. Srinivasan, M. Chaussidon, Constraints on ^{10}Be and ^{41}Ca distribution in the early solar system from ^{26}Al and ^{10}Be studies of Efremovka CAIs. *Earth Planet. Sci. Lett.* **374**, 11–23 (2013).
11. S. J. Desch, H. C. Connolly Jr., G. Srinivasan, An interstellar origin for the beryllium 10 in calcium-rich, aluminum-rich inclusions. *Astrophys. J.* **602**, 528–542 (2004).
12. V. Tatischeff, J. Duprat, N. De Séréville, Light-element nucleosynthesis in a molecular cloud interacting with a supernova remnant and the origin of beryllium-10 in the protosolar nebula. *Astrophys. J.* **796**, 124 (2014).
13. I. Leya, A. N. Halliday, R. Wieler, The predictable collateral consequences of nucleosynthesis by spallation reactions in the early solar system. *Astrophys. J.* **594**, 605–616 (2003).
14. G. J. MacPherson, Calcium-aluminum-rich inclusions in chondritic meteorites. *Treatise Geochem.* **1**, 711 (2003).
15. F. M. Richter, P. E. Janney, R. A. Mendybaev, A. M. Davis, M. Wadhwa, Elemental and isotopic fractionation of Type B CAI-like liquids by evaporation. *Geochim. Cosmochim. Acta* **71**, 5544–5564 (2007).
16. D. S. Ebel, Condensation of rocky material in astrophysical environments. *Meteorites Early Solar Syst. II* **1**, 253–277 (2006).
17. Y. Amelin, A. Kaltenbach, T. Iizuka, C. H. Stirling, T. R. Ireland, M. Petaev, S. B. Jacobsen, U–Pb chronology of the Solar System's oldest solids with variable ^{238}U/^{235}U. *Earth Planet. Sci. Lett.* **300**, 343–350 (2010).
18. A. Bouvier, G. A. Brennecka, M. Wadhwa, Absolute chronology of the first solids in the Solar System. *LPICo* **1639**, 9054 (2011).
19. J. N. Connelly, M. Bizzarro, A. N. Krot, Å. Nordlund, D. Wielandt, M. A. Ivanova, The absolute chronology and thermal processing of solids in the solar protoplanetary disk. *Science* **338**, 651–655 (2012).
20. T. Lee, F. H. Shu, H. Shang, A. E. Glassgold, K. E. Rehm, Protostellar cosmic rays and extinct radioactivities in meteorites. *Astrophys. J.* **506**, 898–912 (1998).
21. P. A. Sossi, F. Moynier, M. Chaussidon, J. Villeneuve, C. Kato, M. Gounelle, Early Solar System irradiation quantified by linked vanadium and beryllium isotope variations in meteorites. *Nat. Astron.* **1**, 0055 (2017).
22. P. H. Warren, Stable-isotopic anomalies and the accretionary assemblage of the Earth and Mars: A subordinate role for carbonaceous chondrites. *Earth Planet. Sci. Lett.* **311**, 93–100 (2011).
23. T. S. Kruijer, C. Burkhardt, G. Budde, T. Kleine, Age of Jupiter inferred from the distinct genetics and formation times of meteorites. *Proc. Natl. Acad. Sci. U.S.A.* **114**, 6712–6716 (2017).
24. S. J. Desch, A. Kalyaan, C. M. D. Alexander, The effect of Jupiter's formation on the distribution of refractory elements and inclusions in meteorites. *Astrophys. J. Suppl. Ser.* **238**, 11 (2018).
25. T. Haugbølle, P. Weber, D. P. Wielandt, P. Benítez-Llambay, M. Bizzarro, O. Gressel, M. E. Pessah, Probing the protosolar disk using dust filtering at gaps in the early solar system. *Astronom. J.* **158**, 55 (2019).
26. L. Yang, F. J. Ciesla, The effects of disk building on the distributions of refractory materials in the solar nebula. *Meteoritics Planet. Sci.* **47**, 99–119 (2012).
27. L. Grossman, S. B. Simon, V. K. Rai, M. H. Thiemens, I. D. Hutcheon, R. W. Williams, A. Galy, T. Ding, A. V. Fedkin, R. N. Clayton, T. K. Mayeda, Primordial compositions of refractory inclusions. *Geochim. Cosmochim. Acta* **72**, 3001–3021 (2008).
28. J. Render, G. A. Brennecka, S. J. Wang, L. E. Wasylenki, T. Kleine, A distinct nucleosynthetic heritage for early solar system solids recorded by Ni isotope signatures. *Astrophys. J.* **862**, 26 (2018).
29. K. R. Bermingham, N. Gussone, K. Mezger, J. Krause, Origins of mass-dependent and mass-independent Ca isotope variations in meteoritic components and meteorites. *Geochim. Cosmochim. Acta* **226**, 206–223 (2018).
30. A. M. Davis, J. Zhang, N. D. Greber, J. Hu, F. L. Tissot, N. Dauphas, Titanium isotopes and rare earth patterns in CAIs: Evidence for thermal processing and gas-dust decoupling in the protoplanetary disk. *Geochim. Cosmochim. Acta* **221**, 275–295 (2018).
31. B. L. A. Charlier, F. L. H. Tissot, N. Dauphas, C. J. N. Wilson, Nucleosynthetic, radiogenic and stable strontium isotopic variations in fine- and coarse-grained refractory inclusions from Allende. *Geochim. Cosmochim. Acta* **265**, 413–430 (2019).
32. Q. R. Shollenberger, A. Wittke, J. Render, P. Mane, S. Schuth, S. Weyer, N. Gusson, M. Wadhw, G. A. Brennecka, Combined mass-dependent and nucleosynthetic isotope variations in refractory inclusions and their mineral separates to determine their original Fe isotope compositions. *Geochim. Cosmochim. Acta* **263**, 215–234 (2019).
33. K. Lodders, Solar system abundances and condensation temperatures of the elements. *Astrophys. J.* **591**, 1220–1247 (2003).
34. S. G. Nielsen, D. Bekaert, T. Magna, K. Mezger, M. Auro, The vanadium isotope composition of Mars: Implications for planetary differentiation in the early solar system. *Geochem. Perspect. Lett.* **15**, 35–39 (2020).
35. P. J. Patchett, Sr isotopic fractionation in Ca–Al inclusions from the Allende meteorite. *Nature* **283**, 438–441 (1980).
36. T. R. Ireland, B. Fegley Jr., The solar system's earliest chemistry: Systematics of refractory inclusions. *Int. Geol. Rev.* **42**, 865–894 (2000).
37. W. V. Boynton, Fractionation in the solar nebula: Condensation of yttrium and the rare earth elements. *Geochim. Cosmochim. Acta* **39**, 569–584 (1975).
38. E. T. Dunham, M. Wadhwa, S. J. Desch, R. L. Hervig, Best practices for determination of Initial ^{10}Be/^{9}Be in early solar system materials by secondary ion mass spectrometry. *Geostand. Geoanal. Res.* **44**, 695–710 (2020).
39. E. Rotenberg, D. W. Davis, Y. Amelin, S. Ghosh, B. A. Bergquist, Determination of the decay-constant of ^{87}Rb by laboratory accumulation of ^{87}Sr. *Geochim. Cosmochim. Acta* **85**, 41–57 (2012).
40. F. Moynier, J. I. Simon, F. A. Podosek, B. S. Meyer, J. Brannon, D. J. DePaolo, Ca isotope effects in Orgueil leachates and the implications for the carrier phases of ^{54}Cr anomalies. *Astrophys. J. Lett.* **718**, L7–L13 (2010).
41. B. L. A. Charlier, G. M. Nowell, I. J. Parkinson, S. P. Kelley, D. G. Pearson, K. W. Burton, High temperature strontium stable isotope behaviour in the early solar system and planetary bodies. *Earth Planet. Sci. Lett.* **329**, 31–40 (2012).
42. D. A. H. Teagle, M. J. Bickle, J. C. Alt, Recharge flux to ocean-ridge black smoker systems: A geochemical estimate from ODP Hole 504B. *Earth Planet. Sci. Lett.* **210**, 81–89 (2003).
43. J. Prytulak, S. G. Nielsen, D. A. Ionov, A. N. Halliday, J. Harvey, K. A. Kelley, Y. L. Niu, D. W. Peate, K. Shimizu, K. W. W. Sims, The stable vanadium isotope composition of the mantle and mafic lavas. *Earth Planet. Sci. Lett.* **365**, 177–189 (2013).
44. J. Pape, K. Mezger, A. S. Bouvier, L. P. Baumgartner, Time and duration of chondrule formation: Constraints from ^{26}Al-^{26}Mg ages of individual chondrules. *Geochim. Cosmochim. Acta* **244**, 416–436 (2019).
45. J. Bollard, J. N. Connelly, M. J. Whitehouse, E. A. Pringle, L. Bonal, J. K. Jørgensen, Å. Nordlund, F. Moynier, M. Bizzarro, Early formation of planetary building blocks inferred from Pb isotopic ages of chondrules. *Sci. Adv.* **3**, e1700407 (2017).
46. C. Burkhardt, N. Dauphas, U. Hans, B. Bourdon, T. Kleine, Elemental and isotopic variability in solar system materials by mixing and processing of primordial disk reservoirs. *Geochim. Cosmochim. Acta* **261**, 145–170 (2019).
47. J. A. M. Nanne, F. Nimmo, J. N. Cuzzi, T. Kleine, Origin of the non-carbonaceous–carbonaceous meteorite dichotomy. *Earth Planet. Sci. Lett.* **511**, 44–54 (2019).
48. S. G. Nielsen, M. Auro, K. Righter, D. Davis, J. Prytulak, F. Wu, J. D. Owens, Nucleosynthetic vanadium isotope heterogeneity of the early solar system recorded in chondritic meteorites. *Earth Planet. Sci. Lett.* **505**, 131–140 (2019).
49. S. S. Hopkins, J. Prytulak, J. Barling, S. S. Russell, B. J. Coles, A. N. Halliday, The vanadium isotopic composition of lunar basalts. *Earth Planet. Sci. Lett.* **511**, 12–24 (2019).

50. D. Clayton, *Handbook of Isotopes in the Cosmos: Hydrogen to Gallium* (Cambridge Univ. Press, 2003), vol. 1.
51. E. A. Schauble, First-principles estimates of equilibrium magnesium isotope fractionation in silicate, oxide, carbonate and hexaaquamagnesium(2+) crystals. *Geochim. Cosmochim. Acta* **75**, 844–869 (2011).
52. J. I. Simon, M. K. Jordan, M. J. Tappa, E. A. Schauble, I. E. Kohl, E. D. Young, Calcium and titanium isotope fractionation in refractory inclusions: Tracers of condensation and inheritance in the early solar protoplanetary disk. *Earth Planet. Sci. Lett.* **472**, 277–288 (2017).
53. P. A. Sossi, B. Fegley Jr., Thermodynamics of element volatility and its application to planetary processes. *Rev. Mineral. Geochem.* **84**, 393–459 (2018).
54. F. M. Richter, Timescales determining the degree of kinetic isotope fractionation by evaporation and condensation. *Geochim. Cosmochim. Acta* **68**, 4971–4992 (2004).
55. J. P. Hirth, G. M. Pound, Coefficients of condensation, evaporation and thermal accommodation. *Prog. Mater. Sci.* **11**, 1 (1963).
56. D. S. Ebel, L. Grossman, Condensation in dust-enriched systems. *Geochim. Cosmochim. Acta* **64**, 339–366 (2000).
57. B. J. Wood, D. J. Smythe, T. Harrison, The condensation temperatures of the elements: A reappraisal. *Am. Mineral. J. Earth Planet. Mater.* **104**, 844–856 (2019).
58. B. Fegley Jr., H. Palme, Evidence for oxidizing conditions in the solar nebula from Mo and W depletions in refractory inclusions in carbonaceous chondrites. *Earth Planet. Sci. Lett.* **72**, 311–326 (1985).
59. A. S. Kornacki, B. Fegley Jr., The abundance and relative volatility of refractory trace elements in Allende Ca,Al-rich inclusions: Implications for chemical and physical processes in the solar nebula. *Earth Planet. Sci. Lett.* **79**, 217–234 (1986).
60. A. M. Davis, L. Grossman, Condensation and fractionation of rare earths in the solar nebula. *Geochim. Cosmochim. Acta* **43**, 1611–1632 (1979).
61. J. Y. Hu, N. Dauphas, F. L. H. Tissot, R. Yokochi, T. J. Ireland, Z. Zhang, A. M. Davis, F. J. Ciesla, L. Grossman, B. L. A. Charlier, M. Roskosz, E. E. Alp, M. Y. Hu, J. Zhao, Heating events in the nascent solar system recorded by rare earth element isotopic fractionation in refractory inclusions. *Sci. Adv.* **7**, eabc2962 (2021).
62. F. R. Niederer, D. A. Papanastassiou, Ca isotopes in refractory inclusions. *Geochim. Cosmochim. Acta* **48**, 1279–1293 (1984).
63. S. Huang, J. Farkaš, G. Yu, M. I. Petaev, S. B. Jacobsen, Calcium isotopic ratios and rare earth element abundances in refractory inclusions from the Allende CV3 chondrite. *Geochim. Cosmochim. Acta* **77**, 252–265 (2012).
64. M. Gounelle, M. Chaussidon, C. Rollion-Bard, Variable and extreme irradiation conditions in the early solar system inferred from the initial abundance of ^{10}Be in Isheyevo CAIs. *Astrophys. J. Lett.* **763**, L33 (2013).
65. K. Fukuda, H. Hiyagon, W. Fujiya, N. Takahata, T. Kagoshima, Y. Sano, Origin of the short-lived radionuclide ^{10}Be and its implications for the astronomical setting of CAI formation in the solar protoplanetary disk. *Astrophys. J.* **886**, 34 (2019).
66. K. Fukuda, H. Hiyagon, W. Fujiya, T. Kagoshima, K. Itano, T. Iizuka, N. T. Kita, Y. Sano, Irradiation origin of ^{10}Be in the solar nebula: Evidence from Li-Be-B and Al-Mg isotope systematics, and REE abundances of CAIs from Yamato-81020 CO3.05 chondrite. *Geochim. Cosmochim. Acta* **293**, 187–204 (2021).
67. J. M. Sisterson, K. Kim, A. Beverding, P. A. J. Englert, M. Caffee, A. T. Jull, D. J. Donahue, L. McHargue, C. Castaneda, J. Vincent, R. C. Reedy, Measurement of proton production cross sections of ^{10}Be and ^{26}Al from elements found in lunar rocks. *Nucl. Instrum. Methods Phys. Res., Sect. B* **123**, 324–329 (1997).
68. A. J. Koning, S. Hilaire, M. C. Duijvestijn, TALYS: Comprehensive Nuclear Reaction Modeling, in *Proceedings of the International Conference on Nuclear Data for Science and Technology (AIP Conf. Proc. 769)*, R. C. Haight, Ed. (AIP, 2005), p. 1154.
69. M. C. Liu, K. D. McKeegan, On an irradiation origin for magnesium isotope anomalies in meteoritic hibonite. *Astrophys. J. Lett.* **697**, L145–L148 (2009).
70. M.-C. Liu, L. R. Nittler, C. M. D. Alexander, T. Lee, Lithium–Beryllium–Boron isotopic compositions in meteoritic hibonite: Implications for origin of ^{10}Be and early Solar System irradiation. *Astrophys. J. Lett.* **719**, L99–L103 (2010).
71. N. Dauphas, M. Chaussidon, A perspective from extinct radionuclides on a young stellar object: The Sun and its accretion disk. *Annu. Rev. Earth Planet. Sci.* **39**, 351–386 (2011).
72. E. Jacquet, Beryllium-10 production in gaseous protoplanetary disks and implications for the astrophysical setting of refractory inclusions. *Astron. Astrophys.* **624**, A131 (2019).
73. N. Ouellette, S. J. Desch, M. Bizzarro, A. P. Boss, F. Ciesla, B. Meyer, Injection mechanisms of short-lived radionuclides and their homogenization. *Geochim. Cosmochim. Acta* **73**, 4946–4962 (2009).
74. K. K. Marhas, J. N. Goswami, A. M. Davis, Short-lived nuclides in hibonite grains from Murchison: Evidence for solar system evolution. *Science* **298**, 2182–2185 (2002).
75. M. C. Liu, K. D. McKeegan, J. N. Goswami, K. K. Marhas, S. Sahijpal, T. R. Ireland, A. M. Davis, Isotopic records in CM hibonites: Implications for timescales of mixing of isotope reservoirs in the solar nebula. *Geochim. Cosmochim. Acta* **73**, 5051–5079 (2009).
76. G. J. MacPherson, E. S. Bullock, P. E. Janney, N. T. Kita, T. Ushikubo, A. M. Davis, M. Wadhwa, A. N. Krot, Early solar nebula condensates with canonical, not supracanonical, initial ^{26}Al/^{27}Al ratios. *Astrophys. J. Lett.* **711**, L117–L121 (2010).
77. G. A. Brennecka, C. Burkhardt, G. Budde, T. S. Kruijer, F. Nimmo, T. Kleine, Astronomical context of Solar System formation from molybdenum isotopes in meteorite inclusions. *Science* **370**, 837–840 (2020).
78. M. Audard, P. Ábrahám, M. M. Dunham, J. D. Green, N. Grosso, K. Hamaguchi, J. H. Kastner, Á. Kóspál, G. Lodato, M. Romanova, S. L. Skinner, E. I. Vorobyov, Z. Zhu, Z. Zhu, Episodic accretion in young stars, in *Protostars and Planets VI*, H. Beuther, R. Klessen, C. Dullemond, Th. Henning, Eds. (University of Arizona Press, 2014), p. 387.
79. G. J. MacPherson, Once a CAI, always a CAI: Flare-up-induced episodic fractionation and melting in the Early Solar Nebula, in *Lunar and Planetary Science Conference* (Department of Mineral Sciences, Museum of Natural History, Smithsonian Institution, No. 1964, 2017), p. 2719.
80. K. K. Larsen, D. Wielandt, M. Schiller, A. N. Krot, M. Bizzarro, Episodic formation of refractory inclusions in the Solar System and their presolar heritage. *Earth Planet. Sci. Lett.* **535**, 116088 (2020).
81. F. H. Shu, H. Shang, M. Gounelle, A. E. Glassgold, T. Lee, The origin of chondrules and refractory inclusions in chondritic meteorites. *Astrophys. J.* **548**, 1029–1050 (2001).
82. R. Hueso, T. Guillot, Evolution of protoplanetary disks: Constraints from DM Tauri and GM Aurigae. *Astron. Astrophys.* **442**, 703–725 (2005).
83. C. P. Dullemond, D. Apai, S. Walch, Crystalline silicates as a probe of disk formation history. *Astrophys. J. Lett.* **640**, L67–L70 (2006).
84. F. C. Pignatale, S. Charnoz, M. Chaussidon, E. Jacquet, Making the planetary material diversity during the early assembling of the solar system. *Astrophys. J. Lett.* **867**, L23 (2018).
85. J. E. Lee, E. A. Bergin, J. R. Lyons, Oxygen isotope anomalies of the Sun and the original environment of the solar system. *Meteorit. Planet. Sci.* **43**, 1351–1362 (2008).
86. V. Agra-Amboage, C. Dougados, S. Cabrit, J. Reunanen, Sub-arcsecond [Fe ii] spectro-imaging of the DG Tauri jet-Periodic bubbles and a dusty disk wind? *Astron. Astrophys.* **532**, A59 (2011).
87. R. K. Mishra, K. K. Marhas, Meteoritic evidence of a late superflare as source of ^{7}Be in the early Solar System. *Nat. Astron.* **3**, 498–505 (2019).
88. S. J. Desch, N. Ouellette, Comment on "Li and Be isotopic variations in an Allende CAI: Evidence for the in situ decay of short-lived ^{10}Be and for the possible presence of the short-lived nuclide ^{7}Be in the early solar system," by M. Chaussidon, F. Robert, and KD McKeegan. *Geochim. Cosmochim. Acta* **70**, 5426–5432 (2006).
89. L. Kööp, P. R. Heck, H. Busemann, A. M. Davis, J. Greer, C. Maden, M. M. M. Meier, R. Wieler, High early solar activity inferred from helium and neon excesses in the oldest meteorite inclusions. *Nat. Astron.* **2**, 709–713 (2018).
90. D. York, N. M. Evensen, M. L. Martinez, J. De Basabe Delgado, Unified equations for the slope, intercept, and standard errors of the best straight line. *Am. J. Phys.* **72**, 367–375 (2004).
91. M. Zhai, E. Nakamura, D. M. Shaw, T. Nakano, Boron isotope ratios in meteorites and lunar rocks. *Geochim. Cosmochim. Acta* **60**, 4877–4881 (1996).
92. S. G. Nielsen, J. Prytulak, A. N. Halliday, Determination of precise and accurate ^{51}V/^{50}V isotope ratios by MC-ICP-MS, Part 1: Chemical separation of vanadium and mass spectrometric protocols. *Geostand. Geoanal. Res.* **35**, 293–306 (2011).
93. F. Wu, Y. Qi, H. Yu, S. Tian, Z. Hou, F. Huang, Vanadium isotope measurement by MC-ICP-MS. *Chem. Geol.* **421**, 17–25 (2016).
94. J. Prytulak, P. A. Sossi, A. N. Halliday, T. Plank, P. S. Savage, J. D. Woodhead, Stable vanadium isotopes as a redox proxy in magmatic systems? *Geochem. Perspect. Lett.* **3**, 75–84 (2016).
95. F. Wu, J. D. Owens, T. Huang, A. Sarafian, K. F. Huang, I. S. Sen, T. J. Horner, J. Blusztajn, P. Morton, S. G. Nielsen, Vanadium isotope composition of seawater. *Geochim. Cosmochim. Acta* **244**, 403–415 (2019).
96. S. Schuth, I. Horn, A. Brüske, P. E. Wolff, S. Weyer, First vanadium isotope analyses of V-rich minerals by femtosecond laser ablation and solution-nebulization MC-ICP-MS. *Ore Geol. Rev.* **81**, 1271–1286 (2017).
97. S. G. Nielsen, D. V. Bekaert, M. Auro, Isotopic evidence for the formation of the Moon in a canonical giant impact. *Nat. Commun.* **12**, 1817 (2021).
98. S. G. Nielsen, J. D. Owens, T. J. Horner, Analysis of high-precision vanadium isotope ratios by medium resolution MC-ICP-MS. *J. Anal. At. Spectrom* **31**, 531–536 (2016).
99. J. Prytulak, S. G. Nielsen, A. N. Halliday, Determination of precise and accurate ^{51}V/^{50}V Isotope ratios by multi-collector ICP-MS, Part 2: Isotopic composition of six reference materials plus the allende chondrite and verification tests. *Geostand. Geoanal. Res.* **35**, 307–318 (2011).
100. F. Wu, Y. Qi, M. R. Perfit, Y. Gao, C. H. Langmuir, V. D. Wanless, H. Yu, F. Huang, Vanadium isotope compositions of mid-ocean ridge lavas and altered oceanic crust. *Earth Planet. Sci. Lett.* **493**, 128–139 (2018).

101. B. L. A. Charlier, I. J. Parkinson, K. W. Burton, M. M. Grady, C. J. N. Wilson, E. G. C. Smith, Stable strontium isotopic heterogeneity in the solar system from double-spike data. *Geochem. Persp. Lett.* **4**, 35–40 (2017).
102. C. Deniel, C. Pin, Single-stage method for the simultaneous isolation of lead and strontium from silicate samples for isotopic measurements. *Anal. Chim. Acta* **426**, 95–103 (2001).
103. F. Albarède, B. Beard, Analytical methods for non-traditional isotopes, in *Reviews in Mineralogy and Geochemistry*, J. J. Rosso, Ed. (Mineralogical Society of America, 2004), pp. 113–152.
104. H. R. Marschall, B. D. Monteleone, Boron isotope analysis of silicate glass with very low boron concentrations by secondary ion mass spectrometry. *Geostand. Geoanal. Res.* **39**, 31–46 (2015).
105. H. R. Marschall, T. Ludwig, The Low-Boron contest: Minimising surface contamination and analysing boron concentrations at the ng/g-level by secondary ion mass spectrometry. *Mineral. Petrol.* **81**, 265–278 (2004).
106. T. Ludwig, H. R. Marschall, P. A. E. Pogge von Strandmann, B. M. Shabaga, M. Fayek, F. C. Hawthorne, A secondary ion mass spectrometry (SIMS) re-evaluation of B and Li isotopic compositions of Cu-bearing elbaite from three global localities. *Mineral. Mag.* **75**, 2485–2494 (2011).
107. R. C. Ogliore, G. R. Huss, K. Nagashima, Ratio estimation in SIMS analysis. *Nucl. Instrum. Methods Phys. Res. B* **269**, 1910–1918 (2011).
108. M.-C. Liu, J. Han, A. J. Brearley, A. T. Hertwig, Aluminum-26 chronology of dust coagulation and early solar system evolution. *Sci. Adv.* **5**, eaaw3350 (2019).
109. T. Gregory, T. H. Luu, C. D. Coath, S. S. Russell, T. Elliott, Primordial formation of major silicates in a protoplanetary disc with homogeneous $^{26}Al/^{27}Al$. *Sci. Adv.* **6**, eaay9626 (2020).
110. B. Jacobsen, Q. Z. Yin, F. Moynier, Y. Amelin, A. N. Krot, K. Nagashima, I. D. Hutcheon, H. Palme, ^{26}Al–^{26}Mg and ^{207}Pb–^{206}Pb systematics of Allende CAIs: Canonical solar initial $^{26}Al/^{27}Al$ ratio reinstated. *Earth Planet. Sci. Lett.* **272**, 353–364 (2008).
111. N. T. Kita, Q. Z. Yin, G. J. MacPherson, T. Ushikubo, B. Jacobsen, K. Nagashima, E. Kurahashi, A. N. Krot, S. B. Jacobsen, ^{26}Al-^{26}Mg isotope systematics of the first solids in the early solar system. *Meteorit. Planet. Sci.* **48**, 1383–1400 (2013).
112. K. P. Jochum, D. B. Dingwell, A. Rocholl, B. Stoll, A. W. Hofmann, S. Becker, A. Besmehn, D. Bessette, H.-J. Dietze, P. Dulski, J. Erzinger, E. Hellebrand, P. Hoppe, I. Horn, K. Janssens, G. A. Jenner, M. Klein, W. F. M. Donough, M. Maetz, K. Mezger, C. Müker, I. K. Nikogosian, C. Pickhardt, I. Raczek, D. Rhede, H. M. Seufert, S. G. Simakin, A. V. Sobolev, B. Spettel, S. Straub, L. Vincze, A. Wallianos, G. Weckwerth, S. Weyer, D. Wolf, M. Zimmer, The preparation and preliminary characterisation of eight geological MPI-DING reference glasses for in-situ microanalysis. *Geostand. Newsl.* **24**, 87–133 (2000).
113. K. P. Jochum, B. Stoll, K. Herwig, M. Willbold, A. W. Hofmann, M. Amini, S. Aarburg, W. Abouchami, E. Hellebrand, B. Mocek, I. Raczek, A. Stracke, O. Alard, C. Bouman, S. Becker, M. Dücking, H. Brätz, R. Klemd, D. de Bruin, D. Canil, D. Cornell, C.-J. de Hoog, C. Dalpé, L. Danyushevsky, A. Eisenhauer, Y. Gao, J. E. Snow, N. Groschopf, D. Günther, C. Latkoczy, M. Guillong, E. H. Hauri, H. E. Höfer, Y. Lahaye, K. Horz, D. E. Jacob, S. A. Kasemann, A. J. R. Kent, T. Ludwig, T. Zack, P. R. D. Mason, A. Meixner, M. Rosner, K. Misawa, B. P. Nash, J. Pfänder, W. R. Premo, W. D. Sun, M. Tiepolo, R. Vannucci, T. Vennemann, D. Wayne, J. D. Woodhead, MPI-DING reference glasses for in situ microanalysis: New reference values for element concentrations and isotope ratios. *Geochem. Geophys. Geosyst.* **7**, Q02008 (2006).
114. D. M. Shaw, M. D. Higgins, M. G. Truscott, T. A. Middleton, Boron contamination in polished thin sections of meteorites: Implications for other trace-element studies by alpha-track image or ion microprobe. *Am. Mineral.* **73**, 894–900 (1988).
115. M. Chaussidon, F. Robert, D. Mangin, P. Hanon, E. F. Rose, Analytical procedures for the measurement of boron isotope compositions by ion microprobe in meteorites and mantle rocks. *Geostand. Newslett.* **21**, 7–17 (1997).
116. T. Nakano, E. Nakamura, Boron isotope geochemistry of metasedimentary rocks and tourmalines in a subduction zone metamorphic suite. *Phys. Earth Planet. In.* **127**, 233–252 (2001).
117. M. Rosner, M. Wiedenbeck, T. Ludwig, Composition-induced variations in SIMS instrumental mass fractionation during boron isotope ratio measurements of silicate glasses. *Geostand. Geoanal. Res.* **32**, 27–38 (2008).
118. A. A. Gurenko, V. S. Kamenetsky, Boron isotopic composition of olivine-hosted melt inclusions from Gorgona komatiites, Colombia: New evidence supporting wet komatiite origin. *Earth Planet. Sci. Lett.* **312**, 201–212 (2011).
119. S. Pabst, T. Zack, I. P. Savov, T. Ludwig, D. Rost, S. Tonarini, E. P. Vicenzi, The fate of subducted oceanic slabs in the shallow mantle: Insights from boron isotopes and light element composition of metasomatized blueschists from the Mariana forearc. *Lithos* **132-133**, 162–179 (2012).
120. Q. R. Shollenberger, G. A. Brennecka, Dy, Er, and Yb isotope compositions of meteorites and their components: Constraints on presolar carriers of the rare earth elements. *Earth Planet. Sci. Lett.* **529**, 115866 (2020).
121. M. Rotaru, J. L. Birck, C. J. Allègre, Clues to early solar system history from chromium isotopes in carbonaceous chondrites. *Nature* **358**, 465–470 (1992).
122. F. A. Podosek, U. Ott, J. C. Brannon, C. R. Neal, T. J. Bernatowicz, P. Swan, S. E. Mahan, Thoroughly anomalous chromium in Orgueil. *Meteorit. Planet. Sci.* **32**, 617–627 (1997).
123. N. Dauphas, B. Marty, L. Reisberg, Molybdenum nucleosynthetic dichotomy revealed in primitive meteorites. *Astrophys. J. Lett.* **569**, L139–L142 (2002).
124. H. Hidaka, S. Yoneda, Diverse nucleosynthetic components in barium isotopes of carbonaceous chondrites: Incomplete mixing of s- and r-process isotopes and extinct ^{135}Cs in the early solar system. *Geochim. Cosmochim. Acta* **75**, 3687–3697 (2011).
125. M. Schönbächler, M. Rehkämper, M. A. Fehr, A. N. Halliday, B. Hattendorf, D. Günther, Nucleosynthetic zirconium isotope anomalies in acid leachates of carbonaceous chondrites. *Geochim. Cosmochim. Acta* **69**, 5113–5122 (2005).
126. T. Yokoyama, C. M. D. Alexander, M. Conel, R. J. Walker, Osmium isotope anomalies in chondrites: Results for acid residues and related leachates. *Earth Planet. Sci. Lett.* **291**, 48–59 (2010).
127. T. Yokoyama, Y. Fukami, W. Okui, N. Ito, H. Yamazaki, Nucleosynthetic strontium isotope anomalies in carbonaceous chondrites. *Earth Planet. Sci. Lett.* **416**, 46–55 (2015).
128. L. Reisberg, N. Dauphas, A. Dauphas, D. G. Pearson, R. Gallino, C. Zimmermann, Nucleosynthetic osmium isotope anomalies in acid leachates of the Murchison meteorite. *Earth Planet. Sci. Lett.* **277**, 334–344 (2009).
129. F. Moynier, A. Agranier, D. C. Hezel, A. Bouvier, Sr stable isotope composition of Earth, the Moon, Mars, Vesta and meteorites. *Earth Planet. Sci. Lett.* **300**, 359–366 (2010).
130. L. Qin, R. W. Carlson, C. M. D. Alexander, Correlated nucleosynthetic isotopic variability in Cr, Sr, Ba, Sm, Nd and Hf in Murchison and QUE 97008. *Geochim. Cosmochim. Acta* **75**, 7806–7828 (2011).
131. C. Burkhardt, T. Kleine, N. Dauphas, R. Wieler, Nucleosynthetic tungsten isotope anomalies in acid leachates of the Murchison chondrite: Implications for hafnium-tungsten chronometry. *Astrophys. J. Lett.* **753**, L6 (2012).
132. C. Burkhardt, M. Schönbächler, Intrinsic W nucleosynthetic isotope variations in carbonaceous chondrites: Implications for W nucleosynthesis and nebular vs. parent body processing of presolar materials. *Geochim. Cosmochim. Acta* **165**, 361–375 (2015).
133. M. Fischer-Gödde, C. Burkhardt, T. S. Kruijer, T. Kleine, Ru isotope heterogeneity in the solar protoplanetary disk. *Geochim. Cosmochim. Acta* **168**, 151–171 (2015).
134. M. Desai, J. Giacalone, Large gradual solar energetic particle events. *Living Rev. Sol. Phys.* **13**, 3 (2016).
135. Y. Kamata, K. Koyama, Y. Tsuboi, S. Yamauchi, X-ray analysis of the ρ Ophiuchi dark cloud with ASCA: Source identification, X-ray spectra, and temporal variability. *Publ. Astron. Soc. Jpn.* **49**, 461–470 (1997).
136. E. D. Feigelson, P. Broos, J. A. Gaffney III, G. Garmire, L. A. Hillenbrand, S. H. Pravdo, L. Townsley, Y. Tsuboi, X-ray-emitting young stars in the Orion nebula. *Astrophys. J.* **574**, 258–292 (2002).
137. H. J. Lange, T. Hahn, R. Michel, T. Schiekel, R. Rösel, U. Herpers, H. J. Hofmann, B. Dittrich-Hannen, M. Suter, W. Wölfli, P. W. Kubik, Production of residual nuclei by α-induced reactions on C, N, O, Mg, Al and Si up to 170 MeV. *Appl. Radiat. Isot.* **46**, 93–112 (1995).

Acknowledgments: We thank I. Leya and P. Sossi for their thoughtful reviews and efforts toward improving our manuscript. **Funding:** This study was funded by NASA Emerging Worlds grant NNX16AD36G to S.G.N. and prepared by LLNL under contract DE-AC52-07NA27344 with release number LLNL-JRNL-819045. M.C.L acknowledges the support by the NASA grant 80NSSC20K0759. The UCLA ion microprobe facility is partially supported by a grant from the NSF Instrumentation and Facilities program. **Author contributions:** S.G.N. designed the project. D.V.B., M.A., Q.R.S., M.-C.L., H.M., K.W.B., B.J., A.S., and S.G.N. contributed to the analyses. D.V.B., M.-C.L., and S.G.N. performed the modeling of CAI irradiation. G.J.M. acquired the backscattered electron images of the samples. D.V.B. wrote the initial version of the manuscript. All coauthors commented on the different versions of the paper, and all the authors read and approved the final version. **Competing interests:** The authors declare that they have no competing interests. **Data and materials availability:** All data needed to evaluate the conclusions in the paper are present in the paper and/or the Supplementary Materials.

Submitted 1 February 2021
Accepted 5 August 2021
Published 29 September 2021
10.1126/sciadv.abg8329

Citation: D. V. Bekaert, M. Auro, Q. R. Shollenberger, M.-C. Liu, H. Marschall, K. W. Burton, B. Jacobsen, G. A. Brennecka, G. J. McPherson, R. von Mutius, A. Sarafian, S. G. Nielsen, Fossil records of early solar irradiation and cosmolocation of the CAI factory: A reappraisal. *Sci. Adv.* **7**, eabg8329 (2021).